

Citation for published version:

F. Feng, M. Tuomi, and H. R. A. Jones, 'Agatha: disentangling periodic signals from correlated noise in a periodogram framework, *Monthly Notices of the Royal Astronomical Society*, Vol. 470 (4): 4794-4814, May 2017.

DOI:

<https://doi.org/10.1093/mnras/stx1126>

Document Version:

This is the Published Version.

Copyright and Reuse:

© 2017 The Authors. Published by Oxford University Press on behalf of the Royal Astronomical Society.

Content in the UH Research Archive is made available for personal research, educational, and non-commercial purposes only. Unless otherwise stated, all content is protected by copyright, and in the absence of an open license, permissions for further re-use should be sought from the publisher, the author, or other copyright holder.

Enquiries

If you believe this document infringes copyright, please contact the Research & Scholarly Communications Team at rsc@herts.ac.uk

Agatha: disentangling periodic signals from correlated noise in a periodogram framework

F. Feng,[★] M. Tuomi[★] and H. R. A. Jones

Centre for Astrophysics Research, School of Physics, Astronomy and Mathematics, University of Hertfordshire, College Lane, Hatfield AL10 9AB, UK

Accepted 2017 May 8. Received 2017 May 1; in original form 2017 January 17

ABSTRACT

Periodograms are used as a key significance assessment and visualization tool to display the significant periodicities in unevenly sampled time series. We introduce a framework of periodograms, called ‘Agatha’, to disentangle periodic signals from correlated noise and to solve the two-dimensional model selection problem: signal dimension and noise model dimension. These periodograms are calculated by applying likelihood maximization and marginalization and combined in a self-consistent way. We compare Agatha with other periodograms for the detection of Keplerian signals in synthetic radial velocity data produced for the radial velocity challenge as well as in radial velocity data sets of several Sun-like stars. In our tests, we find Agatha is able to recover signals to the adopted detection limit of the radial velocity challenge. Applied to real radial velocity, we use Agatha to confirm previous analysis of *CoRoT-7* and to find two new planet candidates with minimum masses of 15.1 and 7.08 M_{\oplus} orbiting HD177565 and HD41248, with periods of 44.5 and 13.4 d, respectively. We find that Agatha outperforms other periodograms in terms of removing correlated noise and assessing the significances of signals with more robust metrics. Moreover, it can be used to select the optimal noise model and to test the consistency of signals in time. Agatha is intended to be flexible enough to be applied to time series analyses in other astronomical and scientific disciplines. Agatha is available at agatha.herts.ac.uk.

Key words: methods: data analysis – methods: statistical – techniques: radial velocities – stars: individual: HD 177565, HD 41248, CoRoT-7.

1 INTRODUCTION

Time series analyses based on periodograms have been created and developed over decades to satisfy different requirements for the detection of periodic phenomena. To analyse unevenly sampled time series in the frequency domain, Lomb (1976) and Scargle (1982) independently developed the so-called Lomb–Scargle (LS) periodogram based on a least-squares fit of sinusoids to data. Variations of the LS periodogram have been developed to account for measurement errors (Gilliland & Baliunas 1987; Irwin et al. 1989) or frequency-dependent mean (Cumming, Marcy & Butler 1999; Zechmeister, Kürster & Endl 2009), non-sinusoidal functions (Bretthorst 2001; Cumming 2004) or multiple periodic signals (Anglada-Escudé & Tuomi 2012; Baluev 2013b). In addition to these LS-like periodograms, Bayesian periodograms have been developed to assess the significance of signals using marginalized likelihoods (MLs) when assuming uniform prior densities (Bretthorst 2001; Mortier et al. 2015).

These periodograms are frequently used in time series analyses in disciplines such as astronomy, climatology, biology and geology. In particular, they are used by astronomers, e.g. to detect planetary candidates in the radial velocity (RV) data, to find periodic variations in photometric time series of quasars and to study asteroseismology. Most periodograms account for the white noise by weighting the data using measurement errors. However, noise in time series is typically not white but could be correlated in time or even in other dimensions. In the case of Doppler measurements of stars, the RV noise¹ is typically correlated in time and wavelength (Feng et al. 2017a; hereafter F17). Thus, the white-noise periodograms are insufficient in assessing the significance of a periodic signal in red-noise-dominated time series.

Some periodograms have been created to analyse time series contaminated by correlated noise. For example, Schulz & Mudelsee (2002) developed the ‘RedFit’ algorithm to fit a first-order autoregressive (AR1) process to paleoclimatic data. However, this

¹ Although noise is equivalent to unknown signals, we consider RV variation-induced by stellar activity as noise in the context of detecting exoplanets.

* E-mail: fengfabo@gmail.com (FF); m.tuomi@herts.ac.uk (MT)

periodogram is biased due to the subtraction of the fitted AR1 component from the data rather than fitting the AR1 and sinusoids simultaneously. This problem, caused by subtraction, is frequently mentioned in the field of exoplanet detections (e.g. Tuomi & Jenkins 2012; Anglada-Escudé & Tuomi 2015; Foreman-Mackey et al. 2015). Recently, Hara et al. (2017) have developed a compressed sensing technique to model the RV red noise as a Gaussian process. This periodogram is also biased due to the subtraction of a global mean and/or a noise component from the data during the pre-processing. Moreover, the Gaussian process it employs could interpret signals as noise without proper penalization (Feng et al. 2016). To remove pointing-induced systematics in the *Kepler*'s two-wheeled extension (K2) data, Angus, Foreman-Mackey & Johnson (2016) have developed a new periodogram to account for the linear correlation between the target light curve and selected noise proxies. However, this periodogram ignores the time-correlated noise, and does not select the so-called ‘Goldilocks noise model’ by optimizing the number of noise proxies, which could be important for avoiding false negatives and positives (Feng et al. 2016; F17).

To analyse time series as complex as encountered with RV data, we introduce ‘Agatha’,² a framework of periodogram analyses based on both Frequentist and Bayesian methods. Agatha is intended to offer a number of features: (1) fit the time-correlated noise using the moving average (MA) model, (2) used to compare noise models to select the Goldilocks noise model (Feng et al. 2016), (3) optimization of the frequency-dependent linear trend simultaneously with sinusoids and noise components, (4) wavelength-dependent noise accounted for by fitting a set of linear functions of the ‘differential RVs’ introduced by F17 to the data, (5) assessment of the significance of signals using the Bayes factor (BF) estimated by the Bayesian information criterion (BIC), which is probably the Goldilocks estimator of BF for the RV data (Feng et al. 2016) and (6) production of the so-called ‘moving periodogram’ (F17) to visualize the change of signals with time thus visually testing the consistency of signals.

Although periodograms might not be as robust as Bayesian methods implemented through Markov Chain Monte Carlo (MCMC) in selecting and quantifying signals (e.g. Ford & Gregory 2007; Feng et al. 2016; Fischer et al. 2016), they are computationally efficient and are good at signal visualization. In combination with Bayesian methods, Agatha would greatly improve the efficiency and robustness of signal detections in unevenly sampled time series such as RVs. The code for Agatha is written in R and is available at GitHub: <https://github.com/phillippro/Agatha>. A relevant web app is also developed and is available at agatha.herts.ac.uk.

This paper is structured as follows. We analytically present the formulae for likelihood-optimization and marginalization to construct the Bayes Factor Periodogram (BFP) and the Marginalized Likelihood Periodogram (MLP) in Sections 2 and 3, respectively. In Section 4, these periodograms are combined to form Agatha and are compared with other periodograms for selected RV data set examples. Finally, we discuss and conclude in Section 6.

2 BAYES FACTOR PERIODOGRAM

We define an unevenly sampled time series as $\{(t_i, v_i)\}$, where v_i is the RV measured at time t_i , and $i \in \{1, 2, \dots, N\}$. The basic model

used for finding periodic signals in the time series is

$$\hat{r}_i = A \cos(2\pi f t_i - \phi) + B \sin(2\pi f t_i - \phi) + \gamma + \dot{\gamma} t_i + \sum_{j=1}^{N_I} d_j I_{ij}, \quad (1)$$

where f is the signal frequency, ϕ is an arbitrary phase offset determined by the time reference point,³ γ is the intercept, $\dot{\gamma}$ is the slope characterizing a trend and $\mathbf{d} \equiv \{d_j\}$ characterizes the linear dependency of the time series on N_I noise proxies $\mathbf{I}_j \equiv \{I_{ij} : i \in 1, \dots, N\}$. This model is linear with respect to all other parameters but f .

To account for time-correlated noise in the time series, we introduce the MA model that is one of the best noise models for the detection of Keplerian signals according to the RV challenge results (Tuomi et al. 2013; Dumusque et al. 2017). The full model is

$$\hat{v}_i = \hat{r}_i + \sum_{k=1}^q m_k \exp[-|t_i - t_{i-k}|/\tau](v_{i-k} - \hat{r}_{i-k}), \quad (2)$$

where m_k and τ are the semi-amplitude and time-scale of the correlation between data measured at different times, and $(v_{i-k} - \hat{r}_{i-k})$ is the residual of \hat{r}_{i-k} at t_{i-k} . Actually, the MA model is a simplified Gaussian process since it only accounts for the correlation between previous data points and the current point. Considering that the Gaussian process may be too flexible to properly disentangle signals from the noise (Feng et al. 2016), we use q MA components, i.e. MA(q), to model the red noise. Red noise refers to time-correlated noise that does not include wavelength-dependent noise. The MA(0) model with $\mathbf{d} = 0$ is the white-noise model that accounts for jitter (or excess white noise) and includes a linear trend. Thus, the full model is the white-noise model combined with the MA model and the correlation between RVs and noise proxies.

We assume that the residuals $\{v_i - \hat{v}_i : i \in \{1, \dots, N\}\}$ follow a Gaussian distribution, the likelihood function for model M and data D is

$$\mathcal{L}(\theta) \equiv P(D|\theta, M) = \prod_i \frac{1}{\sqrt{2\pi(\sigma_i^2 + \sigma_j^2)}} \exp\left[-\frac{(v_i - \hat{v}_i)^2}{2(\sigma_i^2 + \sigma_j^2)}\right], \quad (3)$$

where θ is the model parameters, σ_j is a parameter used to model the so-called ‘jitter’ in the time series, and σ_i is the known measurement error of v_i . In reality, we estimate the optimal values of parameters by maximizing the natural logarithm of the likelihood that is

$$\ln \mathcal{L}(\theta) = -\sum_i \frac{\ln[2\pi(\sigma_i^2 + \sigma_j^2)]}{2} - \sum_i \frac{(v_i - \hat{v}_i)^2}{2(\sigma_i^2 + \sigma_j^2)}. \quad (4)$$

However, it is computationally expensive to directly maximize the logarithmic likelihood as a function of many parameters. To make the parameter optimization more efficient, we first express the logarithmic likelihood as a function of $\mathbf{m} = \{m_k\}$, τ and σ_j by analytically maximizing the logarithmic likelihood. We then use the R package ‘minpack.lm’⁴ to maximize the logarithmic likelihood as a function of \mathbf{m} , τ and σ_j . To simplify the calculation, we introduce the following notations:

$$c_{ik} = m_k \exp(-|t_i - t_{i-k}|/\tau), \quad (5)$$

³ Since the sine fit is time-translation invariant, the reference time could be arbitrarily chosen without affecting the power of fit.

⁴ This package is available at <https://CRAN.R-project.org/package=minpack.lm>.

$$v'_i = v_i - \sum_{k=1}^q c_{ik} v_{i-k}. \quad (6)$$

The residual after subtracting \hat{v}_i from v_i is

$$\begin{aligned} \epsilon_i = v'_i - A & \left[\cos(2\pi f t_i - \phi) - \sum_{k=1}^q c_{ik} \cos(2\pi f t_{i-k} - \phi) \right] \\ & - B \left[\sin(2\pi f t_i - \phi) - \sum_{k=1}^q c_{ik} \sin(2\pi f t_{i-k} - \phi) \right] \\ & - \gamma \left(1 - \sum_{k=1}^q c_{ik} \right) - \dot{\gamma} \left(t_i - \sum_{k=1}^q c_{ik} t_{i-k} \right) \\ & - \sum_{j=1}^{N_I} d_j \left(I_{ij} - \sum_{k=1}^q c_{ik} I_{i-k,j} \right). \end{aligned} \quad (7)$$

We further denote

$$\begin{aligned} w'_i &= 1 - \sum_{k=1}^q c_{ik}, \\ c'_i &= \cos(2\pi f t_i - \phi) - \sum_{k=1}^q c_{ik} \cos(2\pi f t_{i-k} - \phi), \\ s'_i &= \sin(2\pi f t_i - \phi) - \sum_{k=1}^q c_{ik} \sin(2\pi f t_{i-k} - \phi), \\ t'_i &= t_i - \sum_{k=1}^q c_{ik} t_{i-k}, \\ I'_{ij} &= I_{ij} - \sum_{k=1}^q c_{ik} I_{i-k,j}, \end{aligned}$$

$$\begin{aligned} W' &= \sum_i \omega_i w'_i, \\ W &= \sum_i 1/(\sigma_i^2 + \sigma_j^2), \end{aligned}$$

$$\begin{aligned} \widehat{Y\bar{Y}} &= \sum_i \omega_i v'_i v'_i, \\ \widehat{Y\bar{C}} &= \sum_i \omega_i v'_i c'_i, \end{aligned}$$

and

$$\begin{aligned} \widehat{Y\bar{S}} &= \sum_i \omega_i v'_i s'_i, & \widehat{S\bar{S}} &= \sum_i \omega_i s'^2_i, \\ \widehat{Y\bar{W}} &= \sum_i \omega_i v'_i w'_i, & \widehat{S\bar{W}} &= \sum_i \omega_i s'_i w'_i, \\ \widehat{Y\bar{T}} &= \sum_i \omega_i v'_i t'_i, & \widehat{S\bar{T}} &= \sum_i \omega_i s'_i t'_i, \\ \widehat{Y\bar{I}_j} &= \sum_i \omega_i v'_i I'_{ij}, & \widehat{S\bar{I}_j} &= \sum_i \omega_i s'_i I'_{ij}, \\ \widehat{Y\bar{I}_j} &= \sum_i \omega_i v'_i I'_{ij}, & \widehat{W\bar{W}} &= \sum_i \omega_i w'^2_i, \\ \widehat{C\bar{C}} &= \sum_i \omega_i c'^2_i, & \widehat{W\bar{T}} &= \sum_i \omega_i w'_i t'_i, \\ \widehat{C\bar{S}} &= \sum_i \omega_i c'_i s'_i, & \widehat{W\bar{I}_j} &= \sum_i \omega_i w'_i I'_{ij}, \\ \widehat{C\bar{W}} &= \sum_i \omega_i c'_i w'_i, & \widehat{T\bar{T}} &= \sum_i \omega_i t'^2_i, \\ \widehat{C\bar{T}} &= \sum_i \omega_i c'_i t'_i, & \widehat{T\bar{I}_j} &= \sum_i \omega_i t'_i I'_{ij}, \end{aligned}$$

$$\widehat{C\bar{I}_j} = \sum_i \omega_i s'_i I'_{ij}, \quad \widehat{I_j\bar{I}_j} = \sum_i \omega_i I'_{ij} I'_{ij},$$

where $\omega_i = 1/(\sigma_i^2 + \sigma_j^2)W$ is the normalized weighting function.

Since the fit of the periodic model is time-translation invariant (Scargle 1982), we adopt $\phi = 0$ for the optimization of parameters. By maximizing the logarithmic likelihood in equation (4), we find the following equation,

$$\begin{pmatrix} \widehat{C\bar{C}} & \widehat{C\bar{S}} & \widehat{C\bar{W}} & \widehat{C\bar{T}} & \widehat{C\bar{I}_1} & \dots & \widehat{C\bar{I}_{N_I}} \\ \widehat{C\bar{S}} & \widehat{S\bar{S}} & \widehat{S\bar{W}} & \widehat{S\bar{T}} & \widehat{S\bar{I}_1} & \dots & \widehat{S\bar{I}_{N_I}} \\ \widehat{C\bar{W}} & \widehat{S\bar{W}} & \widehat{W\bar{W}} & \widehat{W\bar{T}} & \widehat{W\bar{I}_1} & \dots & \widehat{W\bar{I}_{N_I}} \\ \widehat{C\bar{T}} & \widehat{S\bar{T}} & \widehat{W\bar{T}} & \widehat{T\bar{T}} & \widehat{T\bar{I}_1} & \dots & \widehat{T\bar{I}_{N_I}} \\ \widehat{C\bar{I}_1} & \widehat{S\bar{I}_1} & \widehat{W\bar{I}_1} & \widehat{T\bar{I}_1} & \widehat{I_1\bar{I}_1} & \dots & \widehat{I_1\bar{I}_{N_I}} \\ \vdots & \vdots & \vdots & \vdots & \vdots & \ddots & \vdots \\ \widehat{C\bar{I}_{N_I}} & \widehat{S\bar{I}_{N_I}} & \widehat{W\bar{I}_{N_I}} & \widehat{T\bar{I}_{N_I}} & \widehat{I_{N_I}\bar{I}_{N_I}} & \dots & \widehat{I_{N_I}\bar{I}_{N_I}} \end{pmatrix} \times \begin{pmatrix} A \\ B \\ \gamma \\ \dot{\gamma} \\ d_1 \\ \vdots \\ d_{N_I} \end{pmatrix} = \begin{pmatrix} \widehat{Y\bar{C}} \\ \widehat{Y\bar{S}} \\ \widehat{Y\bar{W}} \\ \widehat{Y\bar{T}} \\ \widehat{Y\bar{I}_1} \\ \vdots \\ \widehat{Y\bar{I}_{N_I}} \end{pmatrix}. \quad (8)$$

By solving the above equations, we obtain the model parameters as functions of \mathbf{m} , τ and σ_j . Then, the residual expressed in equation (7) and the likelihood in equation (3) are functions of \mathbf{m} , τ and σ_j . We use the Levenberg–Marquardt (LM) optimization algorithm (Levenberg 1944; Marquardt 1963) in order to maximize the logarithmic likelihood to obtain the optimized model parameters and the maximum likelihood.

To assess the significance of signals, we follow Feng et al. (2016) to estimate the BF using the BIC which is equivalent to the maximum likelihood ratio of the periodic model and the noise model. Specifically, we calculate the maximum likelihood for the noise model (i.e. $A = B = 0$) and for the full model for a given period. Then, we calculate the BIC according to

$$\text{BIC} = -2 \ln \mathcal{L}_{\max} + n \ln N, \quad (9)$$

where \mathcal{L}_{\max} is the maximum likelihood, n is the number of free parameters and N is the number of data points (see Kass & Raftery 1995 for details). We calculate the logarithmic BF for a given period using

$$\ln \text{BF}_{10} = \frac{\text{BIC}_0 - \text{BIC}_1}{2}, \quad (10)$$

where BIC_1 and BIC_0 are BICs for the periodic model and the noise model, respectively. If $\ln \text{BF}_{10}$ is larger than 5, the periodic model for a given period is favoured over the noise model and the signal at this period is considered significant. This criterion is based on a comparison of many BF estimators by Feng et al. (2016) and is also recommended by Kass & Raftery (1995).

To calculate the BFP, we evenly sample the frequency from a uniform distribution over $[1/\Delta t_{\max}, 1/\Delta t_{\min}]$ with a step of $1/\Delta t_{\max}$.

In this work, we set $\Delta t_{\min} = 1 \text{ d}^5$ and Δt_{\max} to be the time span of the data, leading to an oversampling of Nyquist frequency typically by a factor of more than 10. The values of these parameters could be changed for different applications. Here, we primarily investigate known signals with periods of longer than a day and prefer to avoid the strong aliases around 1 d. We then calculate $\ln(\text{BF})$ for each frequency/period, and construct the BFP from these logarithmic BFs.

3 MARGINALIZED LIKELIHOOD PERIODOGRAM

Although the BFP penalizes model complexity by applying BIC-estimated BF, it assumes a Gaussian-like posterior for each parameter and treats each parameter equally as a free parameter of the model. But such assumptions are not always valid, especially when the posterior is multimodal. According to the Bayesian theorem, the posterior distribution of parameters θ for a given model M is

$$P(\theta|D, M) = \frac{P(D|\theta, M)P(\theta|M)}{P(D|M)}, \quad (11)$$

where $P(D|M) = \int P(D|\theta, M)P(\theta|M)d\theta$ is the so-called ‘evidence’ or integrated likelihood, $P(D|\theta, M)$ is the likelihood function, and $P(\theta|M)$ is the prior probability density. The evidence ratio of two models is the BF.

Assuming uniform prior distributions for all parameters, the posterior of frequency f is

$$P(f|D, M) \equiv \int P(\theta', \theta_{\text{fix}}, f|D, M)d\theta' \propto \int \mathcal{L}(\theta', \theta_{\text{fix}}, f)d\theta', \quad (12)$$

where θ' are the parameters to be marginalized, namely $\theta' = \{A, B, \gamma, \dot{\gamma}\}$, and $\theta_{\text{fix}} \equiv \{\mathbf{d}, \mathbf{m}, \tau, \sigma_J\}$ are the parameters that are determined by the BFP without including sinusoidal functions in the model. Since the integral of likelihood over θ_{fix} cannot be calculated analytically, we either fix these parameters at their optimized values estimated by the BFP or subtract the BFP-determined noise component (excluding the trend) from the data. We will present the formulae for the former method and then set $\mathbf{d} = 0$ and $\mathbf{m} = 0$ to obtain the formulae for the latter.

We drop the non-exponential term in the expression of the likelihood (see equation 3) because only the relative significance of periodic signals is relevant. Then, the posterior becomes

$$P(f|D, M) \propto \mathcal{E}_{\theta'} \equiv \int \exp \left[-\frac{1}{2} \sum_i \frac{\epsilon_i^2}{\sigma_i^2 + \sigma_J^2} \right], \quad (13)$$

where $\epsilon_i \equiv v_i - \hat{v}_i$. Following Mortier et al. (2015), we eliminate the term $\widehat{C}\widehat{S}$ by setting the phase to be⁶

$$\phi = \frac{1}{2} \tan^{-1} \left(\frac{2\widehat{C}'\widehat{S}'}{\widehat{C}'\widehat{C}' - \widehat{S}'\widehat{S}'} \right), \quad (14)$$

⁵ For synthetic data sets, we set Δt_{\min} slightly larger than 1 to avoid aliases since the real signals are known to us.

⁶ Since $\mathbf{d}, \mathbf{m}, \tau$ are determined by the BFP without using sinusoidal functions, the phase ϕ in the MLP could be different to the value used in the calculation of BFP.

where

$$\widehat{C}'\widehat{C}' = \sum_i \omega_i \left[\cos(2\pi f t_i) - \sum_{k=1}^q c_{ik} \cos(2\pi f t_{i-k}) \right]^2, \quad (15)$$

$$\begin{aligned} \widehat{C}'\widehat{S}' &= \sum_i \omega_i \left[\cos(2\pi f t_i) - \sum_{k=1}^q c_{ik} \cos(2\pi f t_{i-k}) \right] \\ &\times \left[\sin(2\pi f t_i) - \sum_{k=1}^q c_{ik} \sin(2\pi f t_{i-k}) \right], \end{aligned} \quad (16)$$

$$\widehat{S}'\widehat{S}' = \sum_i \omega_i \left[\sin(2\pi f t_i) - \sum_{k=1}^q c_{ik} \sin(2\pi f t_{i-k}) \right]^2. \quad (17)$$

This gives us

$$\begin{aligned} -\frac{1}{2} \sum_i \frac{\epsilon_i^2}{\sigma_i^2} &= W \left\{ -\frac{1}{2} [\widehat{Y}\widehat{Y} + A^2\widehat{C}\widehat{C} + B^2\widehat{S}\widehat{S} + \gamma^2\widehat{W}\widehat{W} \right. \\ &\quad + \dot{\gamma}^2\widehat{T}\widehat{T}] + A\widehat{Y}\widehat{C} + B\widehat{Y}\widehat{S} + \gamma\widehat{Y}\widehat{W} + \dot{\gamma}\widehat{Y}\widehat{T} \\ &\quad - A\gamma\widehat{C}\widehat{W} - A\dot{\gamma}\widehat{C}\widehat{T} - B\gamma\widehat{S}\widehat{W} \\ &\quad \left. - B\dot{\gamma}\widehat{S}\widehat{T} - \gamma\dot{\gamma}\widehat{W}\widehat{T} \right\}. \end{aligned} \quad (18)$$

Since the above integrand is the sum of second-degree polynomials of free parameters, we can integrate the integrand with respect to parameter x by expressing it as $ax^2 + bx + c$, where a , b and c are functions of the model parameters. Following Mortier et al. (2015) and by repeatedly using formula $\int_{-\infty}^{\infty} \exp(ax^2 + bx) = \sqrt{\frac{\pi}{|a|}} \exp(-b^2/4a)$, the integral in equation (13) becomes

$$\mathcal{E}_{\theta'}(f) = \frac{(2\pi)^2}{W^2\sqrt{|V|}} \exp \left[\frac{W}{2\widehat{C}\widehat{C}\widehat{S}\widehat{S}U} \left(X + \frac{G^2}{V} \right) \right], \quad (19)$$

where

$$\begin{aligned} G &= \widehat{C}\widehat{C}\widehat{S}\widehat{S}\widehat{Y}\widehat{T}U - \widehat{Y}\widehat{C}\widehat{C}\widehat{T}\widehat{S}\widehat{S}U - \widehat{Y}\widehat{S}\widehat{S}\widehat{T}\widehat{C}\widehat{C}U + \widehat{C}\widehat{C}\widehat{S}\widehat{S}QR \\ V &= \widehat{C}\widehat{C}\widehat{S}\widehat{S}\widehat{T}\widehat{T}U - \widehat{S}\widehat{S}\widehat{C}\widehat{T}^2U - \widehat{C}\widehat{C}\widehat{S}\widehat{T}^2U - \widehat{C}\widehat{C}\widehat{S}\widehat{S}R^2 \\ X &= \widehat{S}\widehat{S}\widehat{Y}\widehat{C}^2U + \widehat{C}\widehat{C}\widehat{Y}\widehat{S}^2U - \widehat{Y}\widehat{Y}\widehat{C}\widehat{C}\widehat{S}\widehat{S}U + \widehat{C}\widehat{C}\widehat{S}\widehat{S}Q^2 \\ U &= \widehat{W}\widehat{W} - \widehat{C}\widehat{W}^2/\widehat{C}\widehat{C} - \widehat{S}\widehat{W}^2/\widehat{S}\widehat{S} \\ Q &= \widehat{Y}\widehat{W} - \widehat{C}\widehat{W}\widehat{Y}\widehat{C}/\widehat{C}\widehat{C} - \widehat{S}\widehat{W}\widehat{Y}\widehat{S}/\widehat{S}\widehat{S} \\ R &= \widehat{C}\widehat{W}\widehat{C}\widehat{T}/\widehat{C}\widehat{C} + \widehat{S}\widehat{W}\widehat{S}\widehat{T}/\widehat{S}\widehat{S} - \widehat{W}\widehat{T}. \end{aligned}$$

The marginalized posterior/likelihood ratio of the models with frequency f_1 and f_2 is

$$\frac{P(f_1|D, M)}{P(f_2|D, M)} = \frac{\mathcal{E}_{\theta'}(f_1)}{\mathcal{E}_{\theta'}(f_2)}. \quad (20)$$

Following Mortier et al. (2015), we scale the MLs to their maximum value to define the relative ML, namely $\text{ML}/\text{ML}_{\max}$. Since the likelihood is only marginalized over a limited number of parameters, the relative ML is not BF, and is thus not appropriate for assessing signal significance.

As mentioned before, there are two ways to construct an MLP. One method is to optimize the noise model and fix $\mathbf{m}, \tau, \mathbf{d}$ and σ_J at the optimal values, and calculate the relative ML. This approach is called the ‘parameter-fixed’ method. The other method is to optimize the noise model and subtract the optimal model prediction from the data, fix σ_J at the optimal value, set $\mathbf{m} = \mathbf{d} = 0$, and calculate the relative probability. This approach is called the ‘noise-subtracted’ method. However, both methods are biased because the parameters of the correlated noise component are determined for

the null hypothesis and are not marginalized simultaneously with other parameters, probably leading to an underestimation of signal significance. This bias will be discussed in Section 4.5. We calculate the MLP using the noise-subtracted method keeping the parameter-fixed method as an option.

4 APPLICATION OF AGATHA

We combine the BFP and MLP to form Agatha that is able to compare noise models, fit the correlated noise and test the consistency of signals in time. Although the BFP and MLP can be used independently, we suggest to use them in combination with Bayesian methods to analyse irregular time series in the following way.

(i) Select the Goldilocks noise model through optimizing the model parameters by using equation (8) and the LM algorithm, and calculate the logarithmic BF using equations (9) and (10) for model comparison (see Section 4.2).

(ii) Calculate the BFP to select the signals with the highest logarithmic BF (see Sections 4.3, 4.4 and 4.5 for examples).

(iii) Use the selected signal as a guidance for the search of signals by applying posterior sampling implemented by the MCMC method.

(iv) Estimate the parameters for the selected signal based on posterior sampling.

(v) Calculate the BIC-estimated logarithmic BF of k -planet model and $k-1$ -planet model. If logarithmic BF is larger than 5, subtract the best-fitted Keplerian components from the data and calculate the residual BFP to identify the next potential signal (see Sections 4.4 and 4.5).

(vi) Repeat the above three steps until \ln BF is less than 5 and there is no significant signals in the residual BFP.

(vii) Test the consistency of all signals using the BFP-based/MLP-based moving periodogram (see Section 4.6).

To test the validation of Agatha and quantify the signals identified by Agatha, we use the Bayesian method implemented by posterior sampling through the adaptive Metropolis (AM) algorithm (Haario et al. 2006). We use uniform prior over the logarithmic scale for time parameters and use uniform priors for other parameters. Following Tuomi (2012), we confirm the existence of a signal if the posterior distribution over the period can be constrained from above and below. We also calculate the BIC-based BFs and adopt a logarithmic BF threshold of 5 to select signals. The reader is referred to Tuomi et al. (2013) and Feng et al. (2016) for details of the AM method. In the following subsections, we will specify how Agatha is used for different applications in data analyses of RV data.

4.1 Data

We have investigated a number of different RV data sets with Agatha during its development, for example F17. Here, we select example synthetic and real RV data sets in order to present the algorithms and methodology behind the usage of Agatha.

To see the improvement of periodograms by inclusion of activity indices, we compare periodograms for the 492 synthetic data points of the second RV challenge data set due to the strong correlation between RVs and indices and because the injected 75.28 d signal is at the limits of detectability (Dumusque 2016). It has also been analysed using compressed sensing techniques by Hara et al. (2017). Five signals corresponding to the five planets in the Kepler-20 system are injected into simulated noise sampled according to the observational calendar of HARPS measurements of τ Ceti. The

periods of these signals are 3.77, 5.79, 10.64, 20.16 and 75.28 d with semi-amplitudes of 2.75, 0.27, 2.85, 0.34 and 1.35 m s⁻¹. The simulated rotation period is 25.05 d.

To see the difference between red-noise and white-noise periodograms, we choose the 221 HARPS RVs of HD41248 because this data set has been the subject of some debate in the literature (e.g. Jenkins et al. 2013; Jenkins & Tuomi 2014; Santos et al. 2014). It presents a good-sized data set with a reasonable sampling of observational times. The data for HD41248 is essentially the same as that used by Jenkins & Tuomi (2014) although we reprocessed using the Template-Enhanced Radial velocity Reanalysis Application (TERRA) algorithm (Anglada-Escudé & Butler 2012) and make use of the wavelength-dependent data, which is available in the appendix.

The data set for HD177565 is chosen as a fairly typical in terms of number of points and phase coverage and with no signals previously reported. It is chosen to illustrate the necessity of modelling wavelength-dependent noise in the detection of weak signals. We present the 68 HARPS data points of HD177565 in Appendix. The data is reduced using the TERRA algorithm that produces RVs for each individual spectral order.

To model the wavelength-dependent noise, F17 have linearly included the RV differences between spectral orders into the model to be used as noise proxies. Specifically, we evenly divide the spectral orders into groups and average the orders in each group to form the so-called ‘aperture data sets’. For n -summations of orders, we thus create n aperture data sets denoted by ‘ $nAPi$ ’, where $i \in \{1, 2, \dots, n\}$. Then, the difference between aperture data sets are called ‘differential RVs’, named by ‘ $nAPi-j$ ’, where $i \in \{2, \dots, n\}$ and $j = i - 1$.

To remove the instrumental bias of HARPS, we generate aperture data sets from a set of 168 HARPS data sets measured for different targets, remove the outliers and stack them to generate the so-called ‘calibration data sets’ (Feng et al. 2017b). We derive aperture data sets and differential RVs from these HARPS measurements, and combine them. Specifically, we remove the (differential) RVs that have absolute values larger than 20 m s⁻¹ or deviate from the mean more than 5σ before combining them. For each epoch in each aperture data set for a target, we average the calibration (differential) RVs measured within the same night by weighting them according to their measurement errors. We further remove the outliers that deviate from the mean more than 3σ . There are also epochs where no RVs of other stars are available, we assign the (differential) RVs measured at nearby epochs to them. We use these calibration data sets as proxies like activity indices to remove instrumental noise. For example, we can use a linear combination of the 1AP1, 3AP2-1 and 3AP3-2 calibration data sets to model the instrumental noise in the 1AP1 data set. We use ‘ $nAPi$ ’ and ‘ $nAPi-j$ ’ to denote the $nAPi$ and $nAPi-j$ calibration data sets. Since the c3AP2-1 data set is found to be strongly correlated with RVs, it is linearly included into the full model in equation (2). Hereafter, we use this calibration data in the noise model for real RV data sets.

4.2 Model comparison

Using the BF as a metric, Bayesian inference can be used to compare models on the same footing. However, because the posterior is typically complex and multimodal, it is difficult to calculate the BF analytically. Therefore, the BF is usually calculated in a Monte Carlo fashion by posterior sampling. In previous work, we have used the posterior samplings to decide which noise model is the optimal one for modelling RV noise (F17; Feng et al. 2017b).

Table 1. The logarithmic BFs of noise models calculated using the BFP and AM methods for the HARPS data set of HD41248 and HD177565. The BFs are calculated with respect to the noise model with $\{q, N_{\text{AP}}\} = \{0, 1\}$. The BFs of the optimal noise models are shown in boldface.

HD41248				HD177565			
Model	Method			Model	Method		
q	N_{AP}	BFP	AM	q	N_{AP}	BFP	AM
0	1	0	0	0	1	0	0
0	3	-0.781	-1.40	0	3	12.6	11.8
0	6	-5.4	-6.50	0	6	6.96	6.5
1	1	38.4	40.3	1	0	13.2	14.9
1	3	37.9	37.2	1	3	23.1	22.6
1	6	30.9	29.1	1	6	19.4	18.2
2	1	40.7	42.6	3	0	11.1	12.8
2	3	39.0	37.5	3	3	21.6	21.5
2	6	32.2	30.4	3	6	17.8	17.1

The posterior distributions for noise-model parameters are typically unimodal according to our analyses. Thus, the BIC-estimated BF is probably a good approximation of the true value of BF. The BIC-estimated BF is also the most conservative and efficient BF estimator according to the comparison of different BF estimators for synthetic and real RV data sets (Feng et al. 2016). Therefore, based on the BIC-estimated BFs, the BFP is an efficient and valid inference tool for noise model comparison.

Following F17, we compare noise models with different numbers of MA components (q) and differential RVs ($N_{\text{D}} \equiv N_{\text{AP}} - 1$ where $N_{\text{AP}} \in \{1, 3, 6, 9, 18, 72\}$).⁷ For a noise model with a given number of MA components and differential RVs, we adopt different initial values for each parameter, maximize the logarithmic likelihood for each initial value set using the LM algorithm and select the highest likelihood to be used when calculating the BF according to equations (9) and (10).

To find the global likelihood maxima rather than the local maxima in the likelihood distribution, we select initial values of $\ln \tau$ according to a uniform prior with boundaries determined by the minimum difference between observation times and the time span of the time series. For the other parameters, we select the initial values from uniform distributions over intervals determined either by the data or by our prior knowledge. For example, we vary d_j according to a uniform prior distribution over $[-d_{\text{max}}, d_{\text{max}}]$ with $d_{\text{max}} = 2(v_{\text{max}} - v_{\text{min}})/(I_{j,\text{max}} - I_{j,\text{min}})$, where v_{max} and v_{min} are the maximum and minimum of RVs, and $I_{j,\text{max}}$ and $I_{j,\text{min}}$ are the maximum and minimum of I_j , respectively. The reader is referred to Feng et al. (2016) for more details of prior distributions of parameters, although the numerical solution of the maximum likelihood is not sensitive to prior choices. The number of generated initial values is equal to the rounding of $10 + 10(N_{\text{AP}}/3 + 2q)$.

Considering the flexibility of the MA model (Feng et al. 2016), we use a logarithmic BF threshold of 5 to select q . Since the dependence of the data on differential RVs is linear and thus is not as flexible as the MA components, we use a threshold of 2.3 to select N_{AP} . We calculate the BFs with the BFP and AM methods for the HARPS data of HD41248 and HD177565. The linear correlation between RVs and BIS, full width at half-maximum (FWHM) and S -index are included in the noise models. We report the BFs with respect to the white-noise model (i.e. $q = 0$ and $N_{\text{AP}} = 1$) in Table 1. We find that the logarithmic BFs calculated using the BFP and AM

typically differ less than 1, confirming the validation of using the BFP as a model comparison tool. According to the BF thresholds we have mentioned, the optimal numbers of MA components and differential RVs are $\{q, N_{\text{AP}}\} = \{1, 1\}$ and $\{1, 3\}$ for HD41248 and HD177565, respectively. We will apply these Goldilocks noise models to the HARPS data in Sections 4.4 and 4.5. In principle, the activity indices of BIS, FWHM and S -index can also be compared in a similar fashion. But to be simple, we combine all of them with differential RVs linearly in the following subsections. We also include c3AP3-2 linearly in the model in Sections 4.4, 4.5 and 4.6.

4.3 Periodograms for index-dependent noise

Periodogram analysis without accounting for the dependence of RVs on activity indices would be misleading if the dependence was strong. Although the linear dependence can be removed from the data before periodogram analysis, the subtraction is biased due to a lack of simultaneous fitting of noise and signals, as demonstrated visually by Anglada-Escudé & Tuomi (2015). We explain this in detail in Section 4.5. The BFP is able to avoid such a bias by optimizing the parameters of noise and signal for each frequency and can thus better determine the maximum likelihood.

To test this, we compare the periodograms of BFP and MLP with the Bayesian generalized Lomb–Scargle (BGLS; Mortier et al. 2015) and generalized Lomb–Scargle (GLS; Zechmeister et al. 2009) periodograms of the second RV challenge data set in Fig. 1. To account for the index-dependent noise, we linearly include all the supplied activity indexes, S -index, BIS and FWHM, in the RV model. To compare periodograms with/without accounting for indices, we use a white-noise model by setting $q = 0$ and $N_{\text{AP}} = 1$. We do not use the red-noise model because we aim to see the improvement of BFP and MLP by including activity indices in the model.

In Fig. 1, we see great improvement in the signal-to-noise ratio of the injected signals for BFP and MLP with respect to those in the BGLS and GLS. Because the parameter of the trend component is optimized/marginalized, the BFP/MLP does not show long-period powers as the BGLS and GLS. The powers corresponding to the signals become unique after accounting for the linear correlation between RVs and indices. In particular, the BF/ML for the rotation period around 25 d is very low compared with the high probability/power in the BGLS/GLS. Although the BGLS and GLS are easy to calculate, the computation of MLP only takes 0.392 s but greatly improves the periodogram. Nevertheless, such a huge improvement is not found for real RV data according to our analyses, indicating unrealistic or oversimplified artificial noise in the synthetic data of Dumusque (2016). This is also part of the reason why we only use the white-noise model in the calculation of BFP and MLP.

In the BFP, the strongest three injected signals at periods of 3.77, 10.64 and 75.28 d with semi-amplitudes of 2.75, 2.85 and 1.35 m s^{-1} all have logarithmic BFs larger than 5 and thus may be identified. These three signals are also the only signals recovered for this data set by the research teams in the RV challenge (Dumusque et al. 2017) though not by all teams. To confirm these three signals further, we subtract the signals from the data sequentially and show the residual BFPs in Fig. 2. We see that the strongest three signals are recovered while the weaker 5.79 and 20.16 d signals can be recovered to a reasonable precision. In particular, the 5.79 d signal is not accurately recovered probably due to an incomplete subtraction of signals or an oversubtraction of the 10.64 d signal that gives rise to a false-positive around its harmonic, 5.3 d. Thus, a detection of harmonics of a known signal probably indicates the existence

⁷ If $N_{\text{AP}} = 1$, the spectral orders are averaged to form one aperture data set. Therefore, there is no differential RVs or $N_{\text{D}} = 0$.

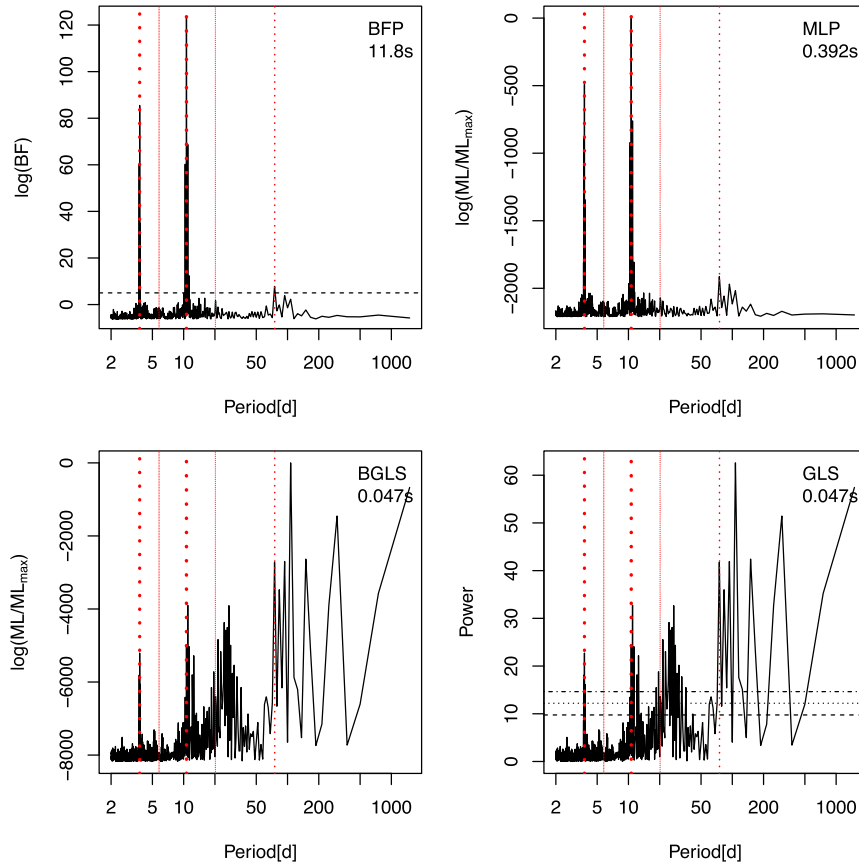


Figure 1. Comparison of the periodograms of BFP, MLP, GLS and BGLS for the white-noise model for the second RV challenge data set with the observational time stamps of τ Ceti. The signals are denoted by red dotted lines and the dot size is proportional to the semi-amplitude of the signal. The horizontal lines in the GLS represent the 0.001, 0.01, 0.1 false alarm probabilities. The logarithmic BF threshold of 5 is shown by the horizontal dashed line. For each periodogram, the CPU time is shown under the periodogram name in the upper-right-hand corner.

of a real signal at a similar period, which is not rare according to the distribution of the period ratio of exoplanets (Steffen & Hwang 2015). Considering this problem of signal subtractions, it should be noted that the BFP is expected to be used in combination with full Bayesian methods to detect signals and that with semi-amplitudes of 0.27 and 0.34 m s^{-1} , these signals are rather weaker than we expect to detect with confidence. Despite not ‘properly’ recovering all the weaker signals in Fig. 2, it is notable that the BFP is able to recover the 1.35 m s^{-1} signal that has a K/N ratio⁸ of 7.6, close to the detection limit of 7.5 according to the analysis of RV challenge results (Dumusque et al. 2017). Thus, our recovery of simulated signals based purely on the BFP is pleasing and realistic, considering that our team has detected signals with K/N as low as 5 without announcing false positives in the RV challenge competition (Dumusque et al. 2017).

4.4 Periodograms for time-correlated noise

As concluded in Baluev (2013a), accounting for red noise in the RV time series is crucial for correctly identifying Keplerian sig-

nals. However, the periodograms used by most researchers in the community are based on the implicit assumption that the noise is white. To overcome this problem, Bayesian methods implemented by various algorithms have been developed to properly model the time and wavelength-correlated noise (e.g. Ford & Gregory 2007, Tuomi et al. 2013; F17). Recently, a framework of Gaussian process is developed to mitigate the red noise caused by stellar activity (Rajpaul et al. 2015). But the Gaussian process is probably too flexible to be the Goldilocks noise model, which avoids both false positives and negatives (Feng et al. 2016). F17 have demonstrated this by comparing different MA models in the Bayesian framework in order to select the Goldilocks noise model.

However, the Bayesian approach is computationally expensive due to the requirement of intensive sampling of the posterior density and computations of integrated likelihoods to estimate BFs. To efficiently account for the red noise as well as to visualize the periodic signals, we use the BFP/MLP to account for red noise in the RV data. In Section 4.2, we show that the noise model with one MA component and without differential RVs is favoured by the HARPS data of HD41248. With this noise model, we calculate the BFP and MLP, and compare them with the GLS and BGLS in Fig. 3.

In this figure, we observe that the ~ 18.4 d signal detected by Jenkins et al. (2013) and Jenkins & Tuomi (2014) is not as significant as a 13.4 d signal in the BFP. The long-period signals appearing in the BGLS, GLS and MLP are strongly weakened in the BFP. We also see that the power of the 26 d signal in the BFP is stronger than

⁸ This signal-to-noise ratio is introduced by Dumusque et al. (2017) to measure the significance of a signal. The K/N ratio for signal with semi-amplitude of K is defined as $K/N \equiv K/RV_{\text{rms}} \times \sqrt{N_{\text{obs}}}$, where RV_{rms} is the standard deviation of RVs after removing the best-fitting trend and correlation with noise proxies and N_{obs} is the number of observations.

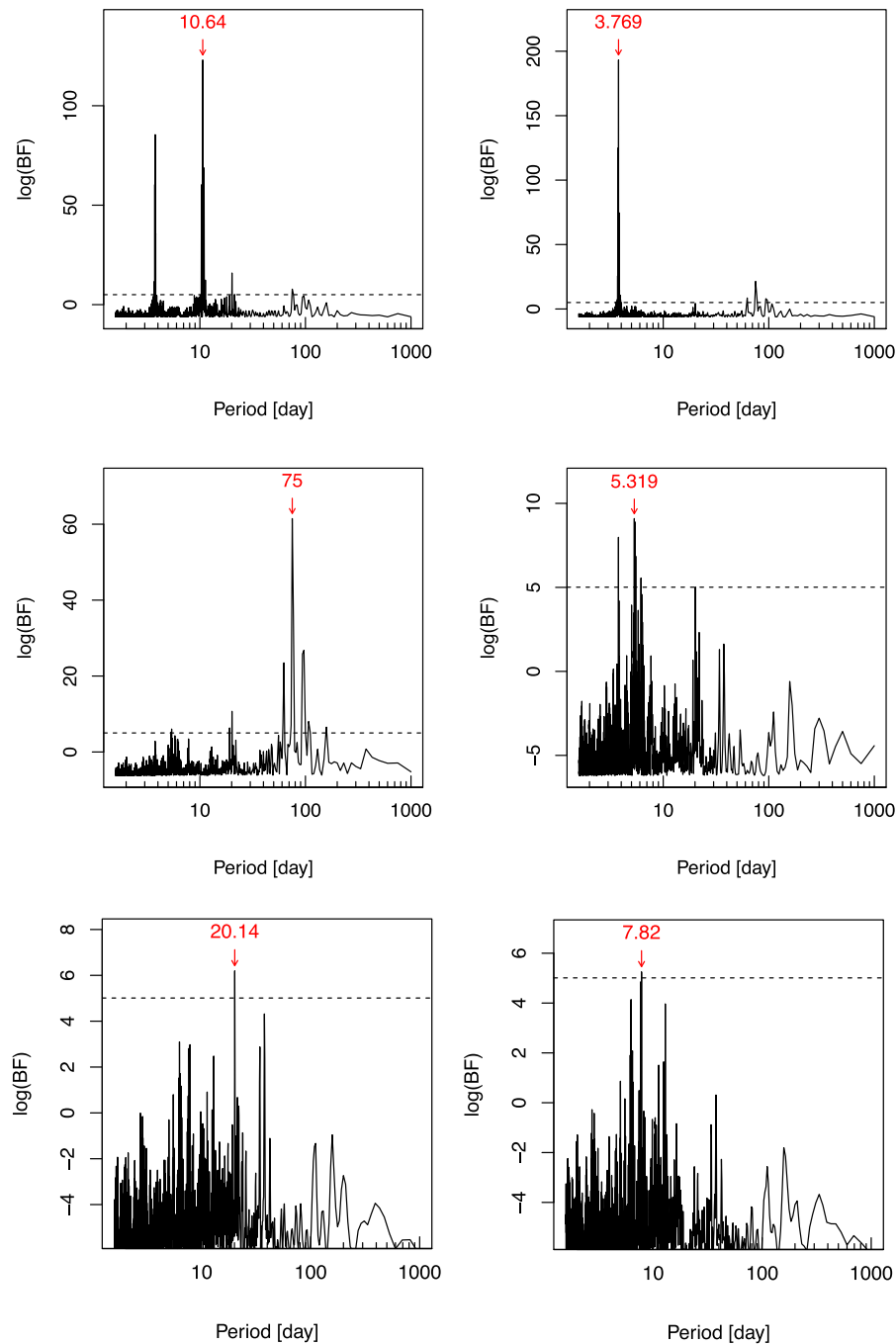


Figure 2. The BFPs of the data (top left) and the residuals after subtracting the first (top right), second (bottom left), third (bottom right), circular signals. To subtract signal precisely, these BFPs are oversampled by a factor of 2 or 3.

that in the other periodograms probably because the red noise in the data would broaden the BF distribution around the signal if it were not accounted for. Although the model used in the calculation of BFP is similar to that used by Jenkins & Tuomi (2014), our results are not sensitive to the choice of noise models since similar signals are identified in different periodograms and are also independently detected by Santos et al. (2014).

To find and compare signals, we subtract signals quantified using the AM posterior sampling from the data, and show the residual BFP in Fig. 4. We see in the top-left panel that the residuals strongly support the existence of the 26 d signal in the data subtracted by the 13.4 d signal. If we subtract the 26 d signal from the data, the

13.4 d one does not disappear, indicating that these two signals are independent signals rather than harmonics of each other, as interpreted by Santos et al. (2014). We further subtract the 13.4 and 26 d signals from the data, and find a signal at a period of about 26.7 d in the residual BFP (see the top-right panel in Fig. 4). This signal is probably caused by an incomplete subtraction of the 26 d signal that corresponds to a rather broad peak in the GLS shown in Fig. 3. This indicates a contribution from stellar noise to this signal, as suggested by previous analyses (Jenkins & Tuomi 2014; Santos et al. 2014).

To compare the 13.4 and 18.4 d signals, we subtract the circular 18.4 d signal from the data because no MCMC chains has identified

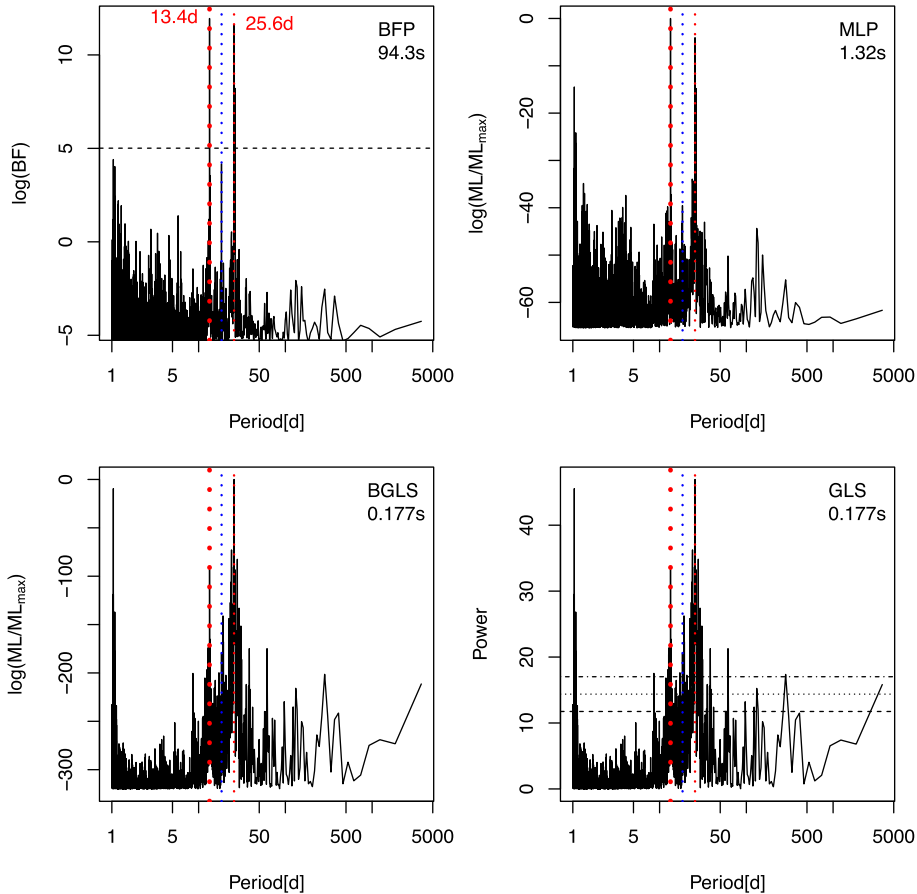


Figure 3. Similar to Fig. 1, but for the first-order MA model combined with the activity indices for the HARPS data set of HD41248. The blue dotted line denotes the 18.4 d planetary candidate reported by Jenkins et al. (2013) based on Bayesian analysis of the same data set. The red dotted lines denote the signal identified by the BFP.

this signal for the one-planet model. We show the residual BFP in the bottom-left-hand panel. We see high BF around 13.4 d, indicating that the 18.4 d signal is probably an alias of the 13.4 d signal. Although we do not find strong signals other than the ~ 26 d one in the top-right-hand panel, we find the third signal at a period of about 290 d using the AM posterior sampling. It increases the logarithmic BF by a factor of 2.5 with respect to the two-planet model, despite a failure in passing the logarithmic BF threshold. However, this signal may be connected to the ~ 26 and 13.4 d signals since $1/(2/25.6 - 1/13.4) = 1/285.9$. The 290 d signal together with the 13.4 and 26 d signals are subtracted from the data to calculate the residual BFP shown in the bottom-right-hand panel of Fig. 4. This residual BFP does not show any significant signals. Thus, there are at most three signals at periods of 13.4, 26 and 290 d in this data set. To study the nature of these signals, we will test their consistency in time in Section 4.6.

4.5 Periodograms for noise correlated in time and wavelength

The noise in RVs is caused not only by stellar activity which is partially recorded by activity indices but also by wavelength-dependent atmospheric and instrumental effects (F17). Previous periodograms do not take the wavelength-dependent noise into account and thus are biased in this respect in terms of identifying potential Keplerian signals. By accounting for differential RVs as additional noise pro-

xies, the BFP and MLP are able to remove the wavelength-dependent noise to a large extent.

To test this, we compare the BFP, MLP, BGLS and GLS for the HARPS RV data set of HD177565. We adopt the noise model including linear functions of activity indices and the 3AP differential RVs. This noise model is favoured by the data based on the BFs calculated both by the AM method and by the BFP (see Table 1). Adopting this noise model, we calculate the BFP, MLP and other periodograms, and show them in Fig. 5. Compared with the other periodograms, 44 d appears to be more prominent in the BFP probably due to the accounting for correlated noise, as shown in Fig. 3. The 44 d signal is not significant in the MLP, indicating a bias introduced by noise subtraction that is mentioned in Sections 3 and 4.3.

To illustrate the relative roles of using an MA model and accounting for differential RVs in reducing noise, we calculate the BFPs for models with $\{q, N_{AP}\} = \{0, 3\}$ and $\{1, 1\}$, and compare them to the previous BFP, top-left in Fig. 6. We observe that the differential RVs play an important role in reducing the wavelength-dependent noise and improve the significance of the ~ 44 d signal. Without dependence on the differential RVs, the BFP would identify a signal at a period of 1.43 d, which is much weaker than the 44 d signal based on the AM-based samplings. On the other hand, the MA model plays a role in reducing the time-correlated noise and the false positive rate. However, based on the difference in the BF ranges of the BFPs, setting $q = 1$ would appear to weaken the signal somewhat

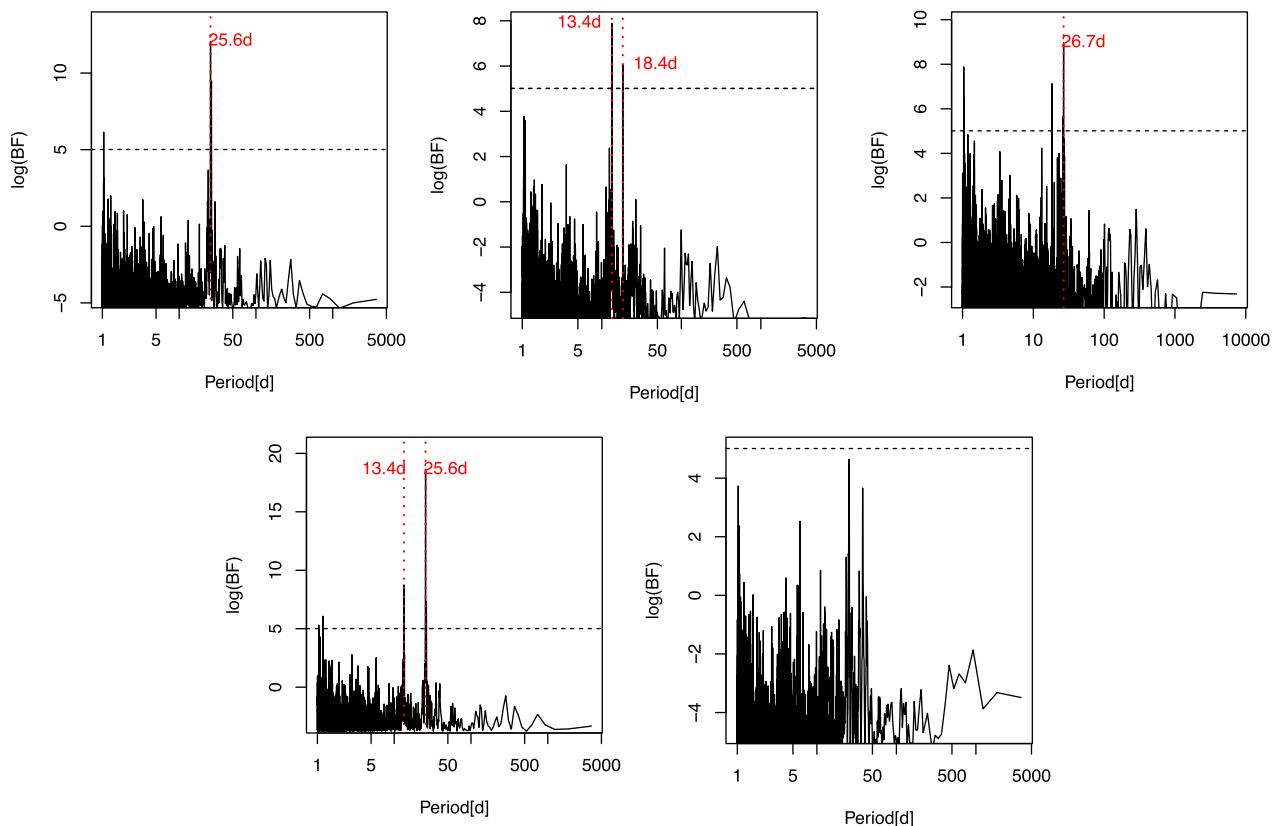


Figure 4. The BFPs for the residuals after subtracting the 13.4 d signal (top left), the 26 d signal (top middle), the 13.4 and 26 d signals (top right), the circular 18.4 d signal (bottom left), the 13.4, 26 and 290.1 d signals (bottom right) from the HARPS data of HD41248.

presumably from part of the periodic variability being interpreted as red noise. Thus as suggested by Feng et al. (2016), the MA model together with other stochastic models should be penalized more than the noise proxies for this noise model comparison. We use the first-order MA model combined with 3AP differential RVs to model the RV noise of HD177565.

To find additional signals, we estimated the parameters for the 44 d signal using AM-based posterior samplings, and subtract the optimal Keplerian component from the data. Then, we calculate the residual BFP and show it in Fig. 7. Based on this residual periodogram, we cannot identify any additional significant signals.

Based on the AM-based posterior samplings, we show the phase-folded data and model predictions in Fig. 8. We observe a reasonable phase coverage for this signal, which corresponds to a planet candidate at a period of about 44 d orbiting HD177565 on a nearly circular orbit. Adopting a stellar mass of $1.0 M_{\odot}$ (da Silva et al. 2012) for HD177565, we further calculate and report the parameters of this signal by tabulating maximum a posteriori (MAP) estimates in Table 2. If this signal is caused by a planet, it has a minimum mass of $15.1 M_{\oplus}$ and semimajor axis of 0.25 au, and thus is a hot Neptune. Notably, there is also a debris disc orbiting HD177565 (Beichman et al. 2006), probably leading to a high impact rate on this planet.

4.6 Moving periodogram

If the semi-amplitude of a periodic signal does not change over time, the signal should be consistently identified in different data chunks

that are data subsets taken at different time intervals. One method for this consistency test is to conduct Bayesian analyses of different data chunks. But this is computationally expensive, and cannot necessarily be applied because of uneven data sampling. An alternative method is to calculate the periodogram of the data within a time window. We move the window with small time steps, and repeat the calculation of periodograms until the whole time span is covered. The assembly of these periodograms forms a 2D periodogram map. This is the so-called ‘moving periodogram’, which has been used in the analysis of *Kepler* light curves by Ramsay et al. (2016) and is introduced in the analysis of RV data here. To make the moving periodogram computationally efficient, we calculate the MLP for each data chunk by subtracting noise component from the data.

For example, we identify two signals at periods of 13.4 and 26 d in the HARPS data of HD41248. We remove the correlated noise component in the two-planet model from the data and calculate the MLP with a white-noise model (or set $m = d = 0$). We calculate the MLP for the data in a 2000 d time window, and move this window to cover the whole time span within 100 steps. We calculate the MLP for each time step, and scale the MLP power to be $RML \equiv (\overline{ML} - \overline{ML}) / (\overline{ML}_{\max} - \overline{ML})$ where \overline{ML} and \overline{ML}_{\max} are the mean and maximum ML. Then, we use colours to encode the RML to calculate the moving periodogram, which is shown in Fig. 9. This periodogram is aimed at visualizing the consistency of signals in time rather than assessing the significance of signals. We can see that the short-period signals are consistently identified over the whole time range while the ~ 290 d signal is visible over about 1000 d centring around JD2455000 and is relatively less distinct at other times.

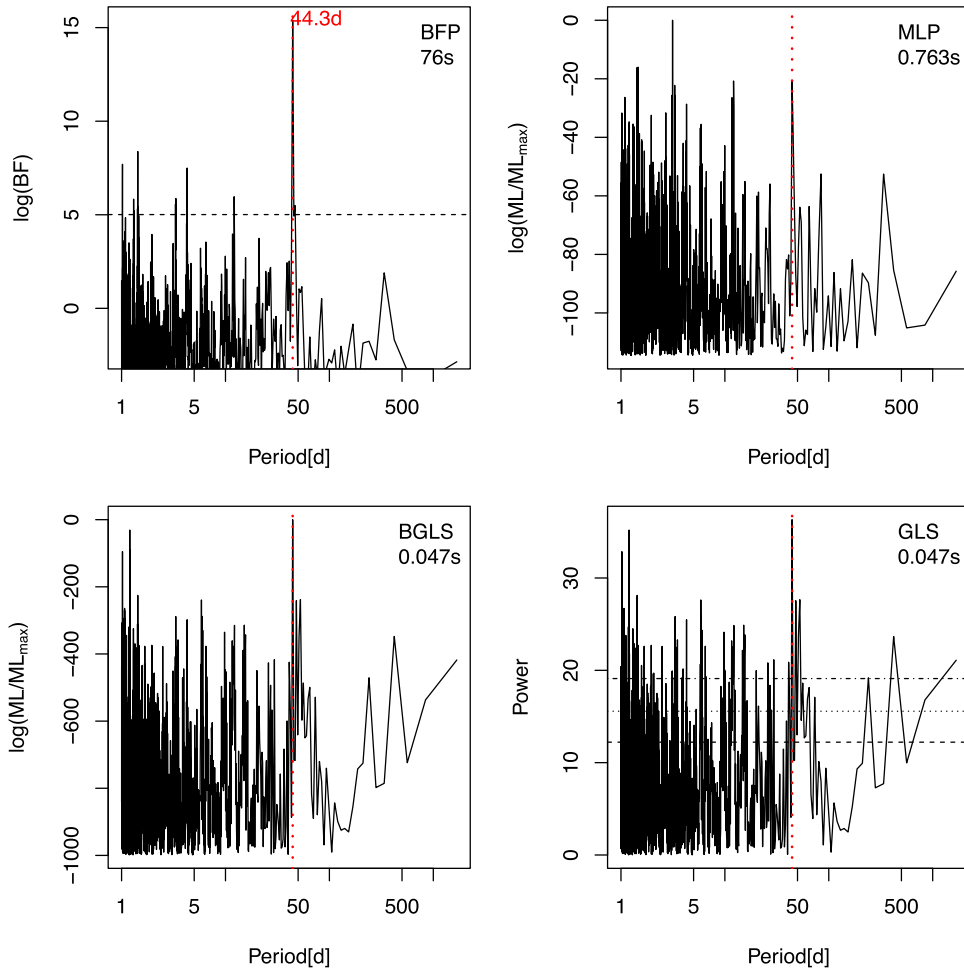


Figure 5. Similar to Fig. 1, but for the model including differential RVs for the HARPS data set of HD177565.

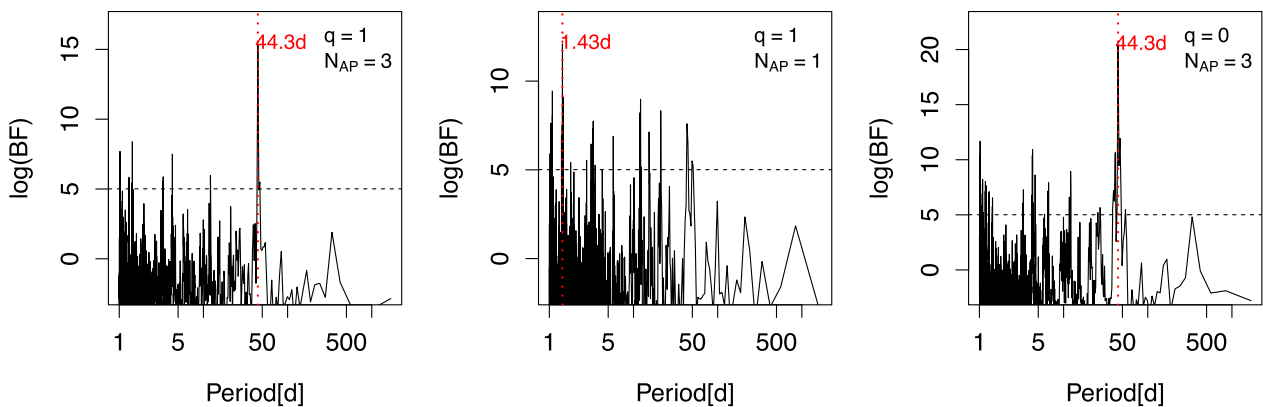


Figure 6. The BFPs for models with $\{q, N_{AP}\} = \{1, 3\}$, $\{1, 1\}$ and $\{0, 3\}$ for HARPS data of HD177565. The signals with maximum BFs are denoted with red dotted lines.

Instead of subtracting the correlated noise from the data, we also calculate the BFP-based periodogram of the original data to account for the possible time-varying noise properties noticed by Santos et al. (2014) and Jenkins & Tuomi (2014). Unlike the MLP-based moving periodogram, the BFP-based one can assess the significance

of signals by encoding the logarithmic BFs with colours. Similar to the MLP-based moving periodogram, the BFP-based moving periodogram is generated from a sequence of BFPs made within a 2000 d moving window. Since the BFP is computationally more expensive than the MLP-based one, we only cover the whole data

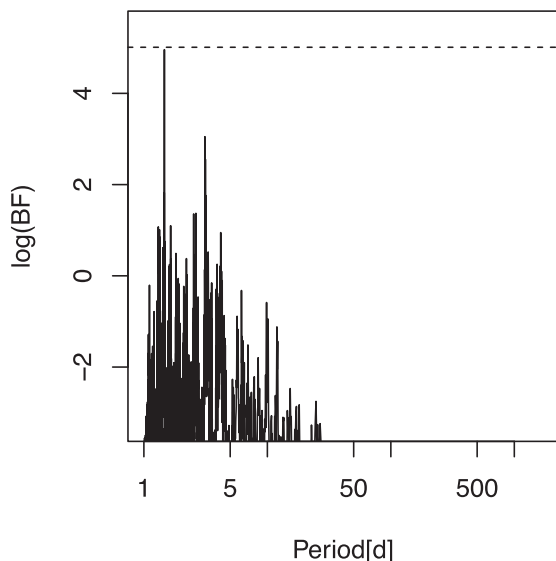


Figure 7. The BFP for the HARPS data of HD177565 with the 44 d signal, subtracted and quantified using the AM posterior sampling.

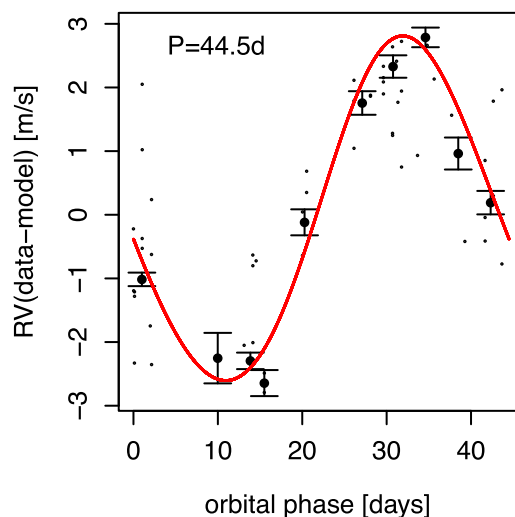


Figure 8. The phase-folded data and the one-planet model prediction for the TERRA-reduced HARPS data of HD177565. The small dots represent raw RVs while the error bars denote the binned data. The noise component is subtracted from the data and the model.

Table 2. The MAP estimation of the parameters for two signals detected in the TERRA-reduced HARPS data of HD177565. The uncertainties of parameters are represented by the values determined at 1 and 99 per cent of the cumulative posterior density. We estimate the minimum planetary mass and semimajor axis using a stellar mass of $1.0 M_{\odot}$ (da Silva et al. 2012) with an assigned 1σ uncertainty of $0.1 M_{\odot}$.

Parameters	HD 177565b
P (d)	44.505 [44.212, 45.091]
K (m s^{-1})	2.71 [1.72, 3.83]
e	0.0593 [0.001 85, 0.231]
ω (rad)	5.41 [0.0679, 6.21]
M_0 (rad)	2.57 [0.0686, 6.23]
$m \sin i$ (M_{\oplus})	15.1 [9.05, 21.5]
a (au)	0.246 [0.227, 0.265]

with 10 steps. We show this moving periodogram in the left-hand panel of Fig. 10. The BFP shows a consistent signal at a period of about 13.4 d. Although the 18.4 d signal also consistently appears in the BFP as noticed by Jenkins & Tuomi (2014), it is not as strong as the 13.4 d signal and the subtraction of the latter makes the former disappear, as shown in Section 4.4. The 26 d signal is not consistently strong over the whole time span, although the high cadence data measured after JD2456000 strongly suggests its existence. According to the analyses in Santos et al. (2014) and Jenkins & Tuomi (2014), this inconsistency of the 26 d signal is probably caused by stellar activity since the periodogram power at this period is seen in the activity indices such as FWHM. This inconsistency could also be caused by the irregular sampling of the data because signals tend to be more significant in high cadence data. In particular, the time sampling would influence the consistency of long-period signals more than that of short-period signals because the former need sampling on longer time series to cover their phase. However, this inconsistency of the 26 d signal is not shown in the MLP-based moving periodogram that does not account for time-varying noise properties. This again demonstrates that the subtraction of a noise component from the data would typically introduce bias in the data analyses.

To check the consistency of the 290 d signal in time, we subtract the Keplerian components of the 13.4 and 26 d signals from the data and show the residual moving periodogram in the right-hand panel of Fig. 10. We see no evidence for strong signals, as indicated by the BF values. On the other hand, the logarithmic BF is relatively high around 18 and 26 d, but is not significant by being higher than 5. The signals apparent in the residual BFs could arise from the subtraction of signals from all data chunks when these signals do not contribute the same amount of RV variation to different data chunks. This is evident from the non-uniform significance of the 26 d signal over time shown in the left-hand panel. Considering the potential bias introduced by signal subtraction, the residual moving periodograms can only be used in combination with Bayesian methods which account for all signals together with the noise model parameters simultaneously.

Considering these factors and the analyses shown in Section 4.4, we conclude that the 13.4 d signal corresponds to a planet candidate, and interpret the 18.4 d signal as an alias of the 13.4 d signal. Following the conclusion in Jenkins & Tuomi (2014), we regard the 26 d signal as a possible combination of a Keplerian signal and stellar rotation. Moreover, the 13.4 and 26 d signals are close to the 1:2 period ratio that is found to be common in extrasolar planetary systems (Steffen & Hwang 2015). We are suspicious about the existence of the 290 d signal since we cannot find it in the residual BFP. We also find that the inclusion of this signal increases the eccentricity of the 26 d signal and changes the phase of the 13.4 d signal, indicating that the 290 d signal is probably a signal connected to the 13.4 and 26 d signals. Moreover, this signal does not satisfy the logarithmic BF threshold of 5.

To visualize the fitting of the 13.4 and 26 d signals quantified by the AM posterior sampling, we show the phase-folded RVs in Fig. 11. We see a good phase coverage, further increasing their credibility as planet candidates. Following Jenkins et al. (2013), we adopt a stellar mass of $0.92^{+0.05}_{-0.05} M_{\odot}$ for HD41248, calculate the parameters of these two signals and report them in Table 3. The parameters we estimate for the 26 d signal are consistent with those found by Jenkins et al. (2013). The 13.4 d planet candidate corresponds to a super-Earth with a minimum mass of $7.08 M_{\oplus}$, and an eccentricity of 0.01, which is lower than the value reported for the 18.4 d signal by Jenkins et al. (2013).

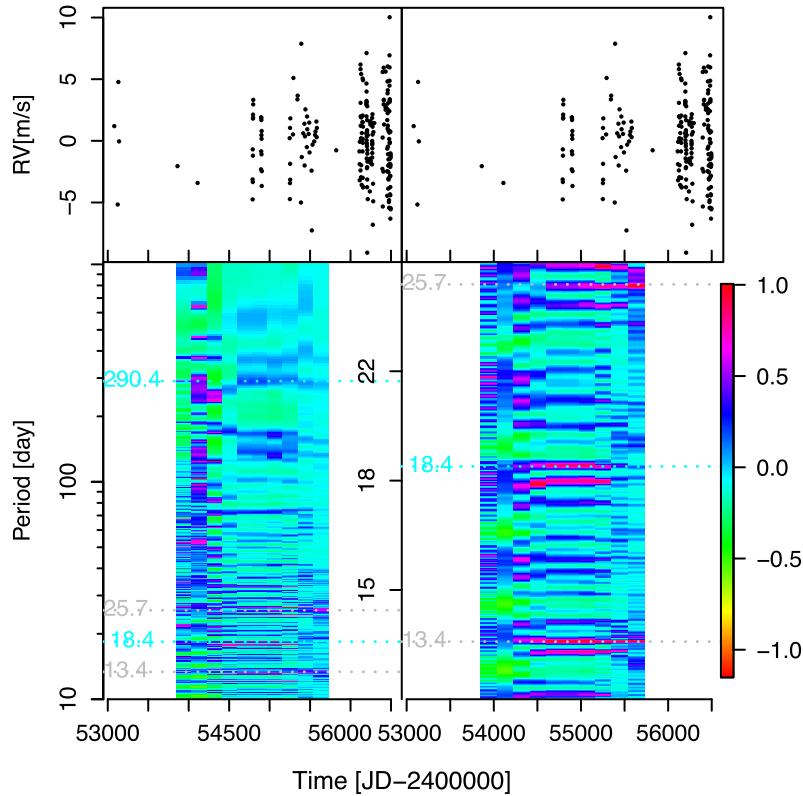


Figure 9. The MLP-based moving periodogram of the HARPS RV data set of HD41248. The periodogram is calculated in a 2000 d moving time window covering the whole time span in 10 steps. The periodogram powers for each step is encoded by colours and shown vertically at the centre of the time window. Thus, the time span of the moving periodogram is shorter than the data time span by 2000 d. The top panels show the noise-subtracted data while the bottom ones show the moving periodogram for period ranging from 10 to 1000 d (left) and for a narrow period range around the short-period signals (right). The colour bar shows the RMLs of the MLP. To optimize the visualization of signals, the RMLs are truncated to $\text{med}(\text{RML}) - 5\sigma_{\text{RML}}$, where $\text{med}(\text{RML})$ and σ_{RML} are the median and standard deviation of RMLs, respectively. The signals are denoted by the grey dotted lines while the signals not identified by the model are denoted by cyan dotted lines.

In summary, the moving periodogram is a useful tool for diagnosing the consistency of signals in time, and in visualizing the change of signals in time. Although the MLP-based moving periodogram is relatively fast to calculate, the BFP-based moving periodogram is more robust in terms of accounting for time-varying noise properties. We expect better performance of the BFP-based moving periodogram due to its ability to account for the trend and correlated noise that vary with observation seasons. The advantage of these new moving periodograms is evident from the analyses of the HARPS data of HD41248. On the other hand, the MCMC-based test of signal consistency is computationally expensive and the divisions of the observational baseline will often be too few for consistency tests. The moving periodograms can provide an alternative and reliable visualization of periodic signals in time series albeit with reliance on careful scaling and visualization and the need for a long-enough observational baseline.

5 ANALYSING THE HARPS DATA OF *CoRoT-7* USING THE AGATHA APP

In this section, we reanalyse the HARPS data of the well-known target, *CoRoT-7*, and show how to use the Agatha app. The data is obtained from the European Southern Observatory archive, and is

processed with the TERRA algorithm (Anglada-Escudé & Butler 2012). Our data is essentially the same as that used by Tuomi et al. (2014). *CoRoT-7* is a moderately active G9 star (Bruntt et al. 2010) hosting two planets with orbital periods of 3.7 and 0.85 d (Léger et al. 2009; Queloz et al. 2009). There is much controversy over the existence of a third planet with a period of about 9 d (Haywood et al. 2014; Tuomi et al. 2014; Mortier & Collier Cameron 2017). We apply the Agatha app to the reanalysis of the HARPS data of *CoRoT-7* as follows.

First, we choose files from the archived data list or upload our own data. Since we have processed the HARPS data of *CoRoT-7* using the TERRA algorithm, we choose it from the list, as seen in Fig. 12. The data file contains the observation times, RV, RV errors and noise proxies including activity indices, calibration data sets and differential RVs.

Then, we compare noise models in the ‘Model Comparison’ tab. The user can choose the data set for noise model comparison, the maximum number of MA components and the type of proxy comparison. The default proxy comparison is ‘Cumulative’, which means that Agatha will first calculate the Pearson correlation coefficients between proxies and RVs. Then, Agatha will add proxies one by one in a decreasing order of coefficients to avoid the inclusion of redundant noise proxies that may correlate with the noise proxies

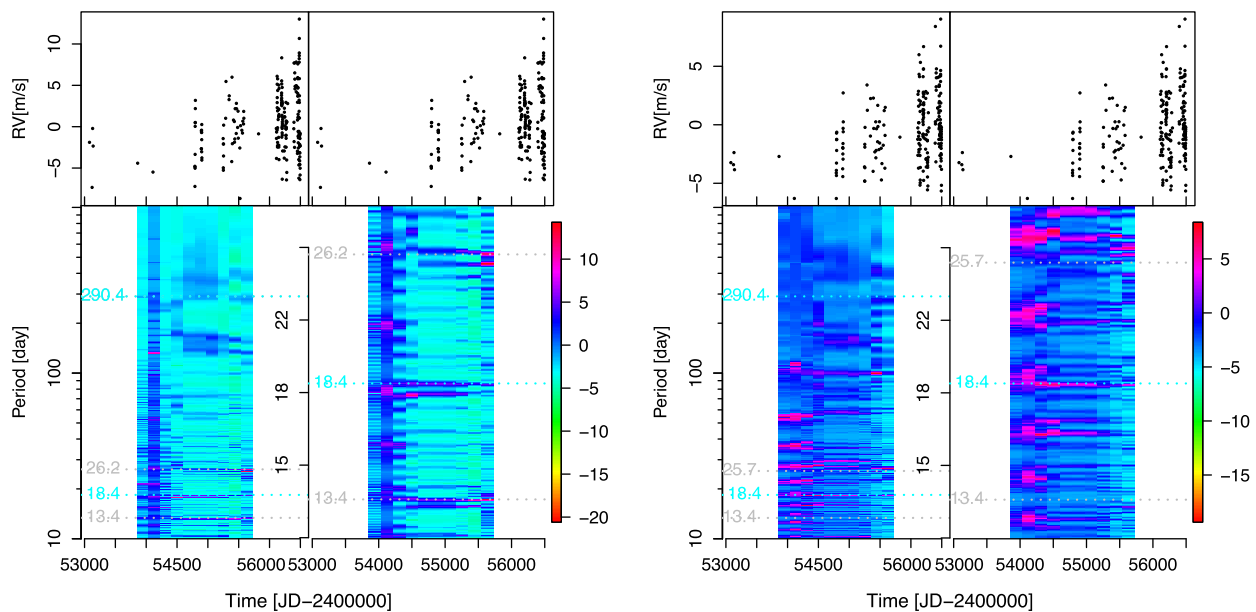


Figure 10. The BFP-based moving periodograms of the HARPS RV data set of HD41248 (left) and the residuals after subtracting the 13.4 and 26 d signals (right). The colour encodes the logarithmic BFs. The logarithmic BFs are truncated to optimize the visualization of signals. The other elements are similar to Fig. 9.

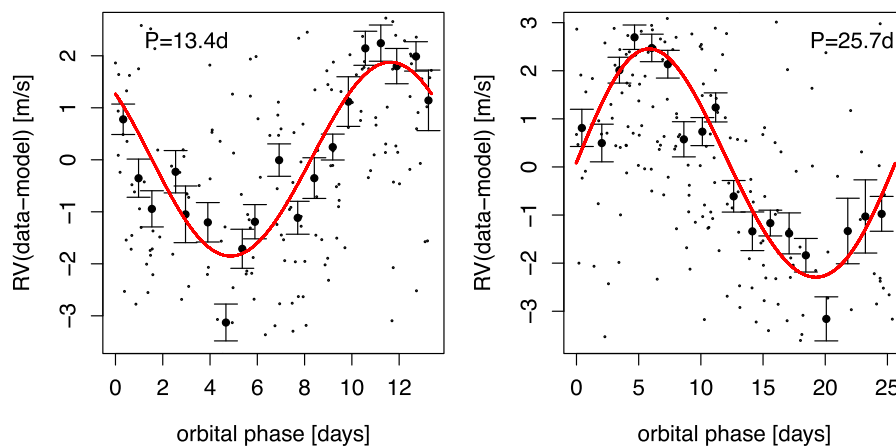


Figure 11. As in Fig. 8, but for the HARPS data of HD41248 and the two significant signals in the data.

Table 3. The MAP estimates of the parameters for two signals detected in the TERRA-reduced HARPS data of HD41248. We are dubious about the existence of HD 41248b due to an approximate overlap between its period and rotation period. We estimate the minimum planetary mass and semimajor axis using a stellar mass of $0.92_{-0.05}^{+0.05} M_{\odot}$ (Jenkins et al. 2013).

Parameters	HD 41248b?	HD 41248c
P (d)	25.654 [25.566, 25.694]	13.365 [13.353, 13.387]
K (m s^{-1})	2.37 [1.30, 2.93]	1.86 [1.03, 2.5]
e	0.0489 [0.002 01, 0.260]	0.0117 [0.002 99, 0.257]
ω (rad)	5.49 [3.26, 9.3]	0.943 [-3.04, 3.04]
M_0 (rad)	5.57 [3.22, 9.33]	6.18 [3.24, 9.31]
$m \sin i$ (M_{\oplus})	8.36 [5.53, 12.8]	7.08 [3.56, 8.83]
a (au)	0.166 [0.159, 0.173]	0.107 [0.103, 0.112]

included in the model. The basic number of proxies is the number of proxies included in the reference model. We set the basic number to be zero and set the maximum number of proxies to be 5. We also set the maximum number of MA components to be 2. Then, we click the ‘compare noise models’ button and get the table of logarithmic BFs as shown in Fig. 13. The user can also download the table for publication.

Based on the logarithmic BF threshold of 5, the optimal noise model is the model that combines MA(1) and a linear function of FWHM. Then, we use this noise model in the calculation of periodograms. There are many types of periodograms available, which can be compared if multiple periodograms are chosen. Since the BFP is the most reliable periodogram, we only choose the BFP to visualize signals. We choose the number of MA components and

Agatha

Disentangling periodic signals from correlated noise in a periodogram framework

CoRoT7_HARPS

Show 25 entries

Time	RV	eRV	BIS.proxy1	FWHM.proxy2
54527.543878	5.36317818963286	1.58019782806528	-10.76786	7.065462221
54530.604318	13.2372756028425	1.61848487811467	-8.94913	7.063339731
54550.503481	-6.78818454132595	2.22731953770212	-16.0835	7.072769733
54775.819119	-4.49383757467924	2.2413667778593	-2.19808	7.10634524
54776.75845	-5.22395563035185	2.8618840630736	-7.8479	7.118732927
54777.761675	1.80271126893704	2.06548712730738	0.999643	7.09913847

Figure 12. The screen shot of choosing files.

Agatha

Disentangling periodic signals from correlated noise in a periodogram framework

CoRoT7_HARPS

Maximum number of MA components: 2

Type of proxy comparison: Cumulative

Basic number of noise proxies: 0

Maximum number of noise proxies: 5

The number of proxies is counted from the fourth column of the data.

compare noise models

Logarithmic BIC-estimated Bayes factor

	white noise	MA(1)	MA(2)
no proxy	0.0	65.9	64.9
proxies: 2	2.6	70.7	69.6
proxies: 2,3	0.2	68.6	67.4
proxies: 2,3,6	1.5	67.1	66.2
proxies: 2,3,6,1	3.4	64.6	63.9
proxies: 2,3,6,1,11	3.6	63.1	62.2

Optimal noise model: MA(1)
Optimal proxies: 2

Download the Bayes Factor table

Figure 13. The screen shot of model comparison.

proxies according to the result of model comparison, and click the button of ‘plot periodograms’ to calculate the BFP. We show the BFP in Fig. 14. The logarithmic BF at 3.7 d is around 30, much larger than the threshold of 5. Hence, we quantify this signal using MCMC-based posterior samplings. We calculate the BFP for the data subtracted by the Keplerian component of the one-planet model and show it in the left-hand panel of Fig. 15. We see a significant

signal around 8.9 d, which is confirmed as a planetary candidate by Tuomi et al. (2014). After subtracting this signal from the data, we calculate the residual BFP that is shown in the right-hand panel of Fig. 15. The signal at 0.85 d is strong in this BFP, which corresponds to the planet detected using the transit method.

Therefore, the combination of Agatha and MCMC methods can identify three signals at periods of about 0.85, 3.7 and 8.9 d, which

Agatha

Disentangling periodic signals from correlated noise in a periodogram framework

About Agatha Choose File Scatter Plot Model Comparison 1D Periodogram 2D Periodogram

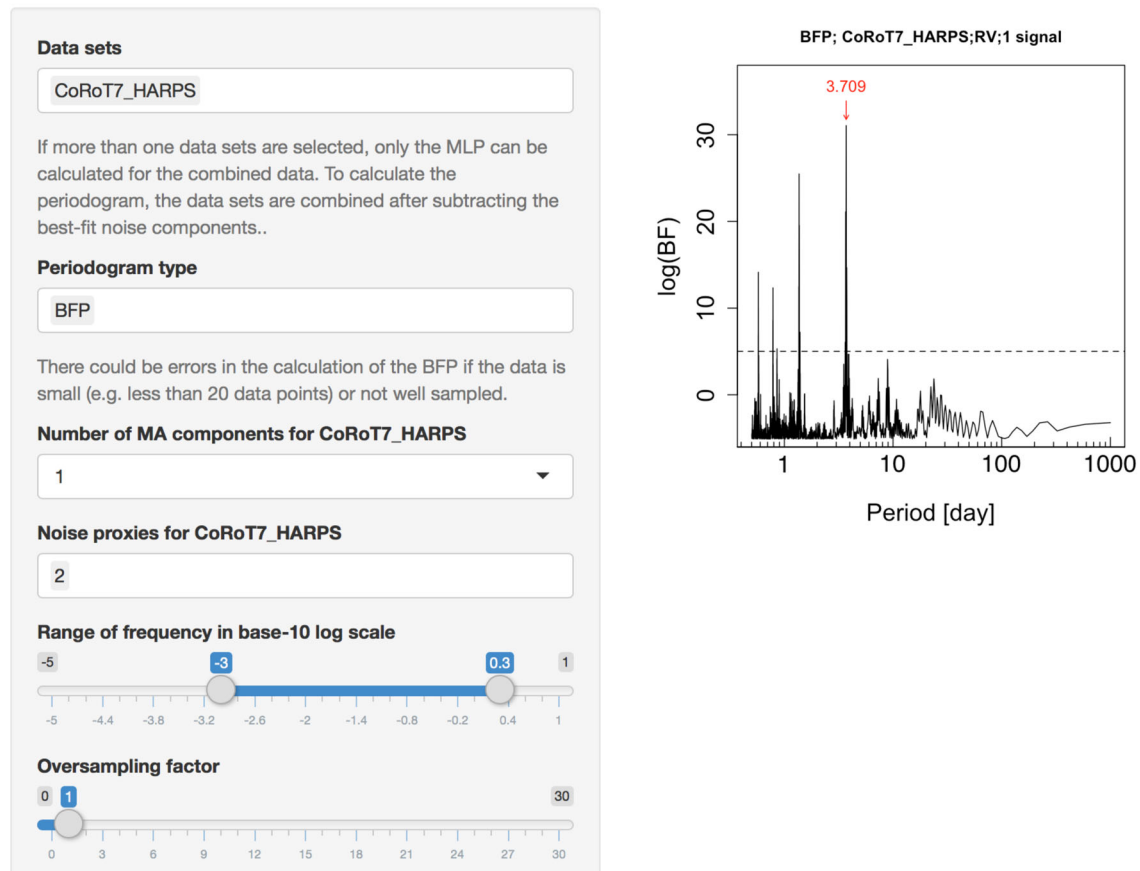


Figure 14. The screen shot of the calculation of BFP.

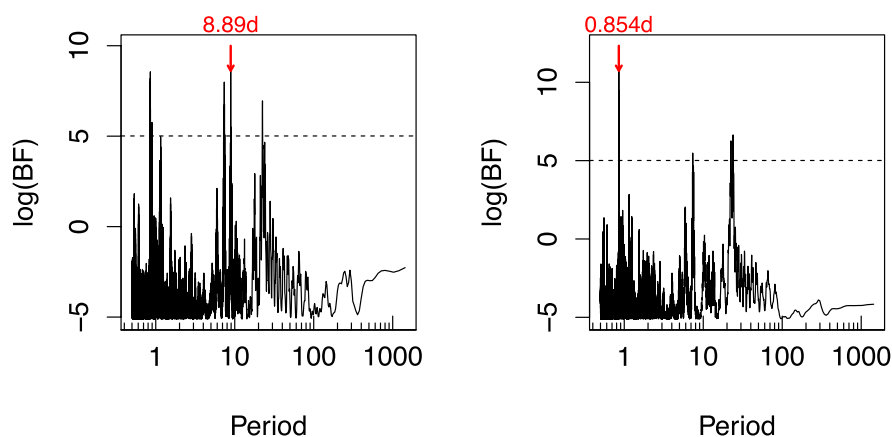


Figure 15. The BFPs of the data subtracted by the Keplerian components of the one-planet (left) and two-planet (right) models quantified using MCMC samplings.

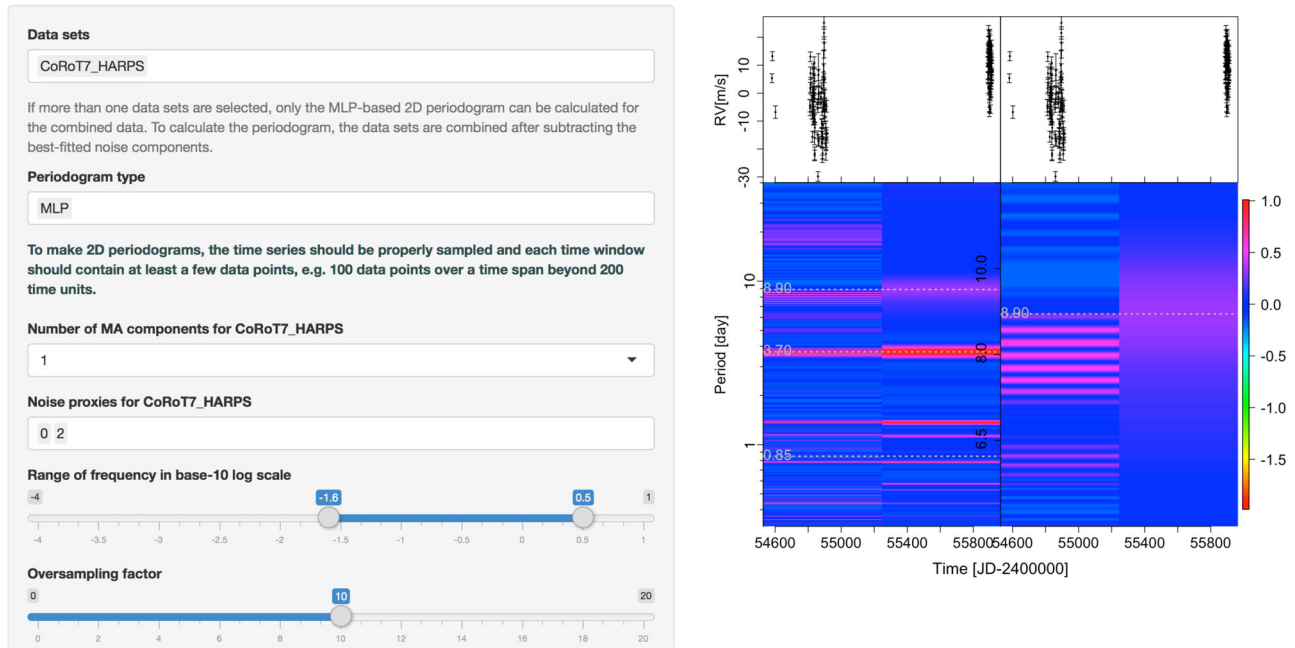
have been confirmed by Tuomi et al. (2014) using the MA(1) model combined with Bayesian methods. But the 8.9 d signal is not confirmed by Haywood et al. (2014) probably due to their usage of Gaussian process, which has been found to interpret signals as noise and thus lead to false negatives (Feng et al. 2016). Such false

negatives could be avoided by using simpler red-noise models such as the MA(1) model. A Bayesian analysis of this data set shows that the inclusion of the 8.9 d signal increases the BIC-estimated BF by a factor of 25 with respect to the two-planet model. This provides weak evidence for its existence, although Kass & Raftery

Agatha

Disentangling periodic signals from correlated noise in a periodogram framework

About Agatha Choose File Scatter Plot Model Comparison 1D Periodogram 2D Periodogram

**Figure 16.** The screen shot of the calculation of moving periodogram.

(1995) consider such an improvement as strong evidence. Moreover, this signal does not overlap with the rotation period that is about 23 d (Queloz et al. 2009). But considering that this signal does not pass the logarithmic BF threshold of 5, we do not interpret it as a planet candidate. This signal is not confirmed by Mortier & Collier Cameron (2017) either based on the stacked BGLS.

We move on to check the consistency of signals in time using the moving periodogram. We choose the periodogram type, the noise model, the time window, the number of steps and other parameters in the ‘2D periodogram’ tab. We calculate the MLP-based moving periodogram in a time window of 300 d covering the data in two steps to avoid the 3-yr gap between the 2009 and 2012 RV campaigns. The periodogram is shown in Fig. 16. As we can see, the signals at periods of 3.7 and 0.85 d are significant while the 8.9 d signal is visible over the whole time span. The location of the periodogram power deviates from 0.85 d probably due to the assumption of circular orbits in the calculation of moving periodogram. Nevertheless, the consistency of signals cannot be fully explored using the moving periodogram because the data size is small and/or the data is not well sampled and so we are not able to be definitive about the consistency of 8.9 d signal in time.

In order to make reliable periodograms, the window size and the period range of the moving periodogram should be adjusted according to the property of a given data set. As a rule of thumb, each bin with more than 10 points spread across the bin can be expected to provide constraints on periods less than the bin size. For example, for 100 RVs uniformly sampled over a time span of 1000 d, we recommend a window size of at least 100 d to include at least 10 points in each window for periodogram calculation. If a 100 d window is adopted, the moving periodogram is only able to check the consistency of signals with periods less than 100 d. For RVs sampled with significant gaps, the number of steps could be

chosen to avoid the gaps to a large extent. For example, we choose two steps to calculate the MLP for the 2009 and 2012 RV campaigns separately (see Fig. 16). The user should vary the time window and steps to optimize the moving periodogram.

In summary, we confirm three signals at periods of 0.85, 3.7 and 8.9 d in the HARPS data of *CoRoT-7*. Based on our analysis of the current HARPS data, nothing definitive can be said regarding the nature of the 8.9 d signal. More and well-sampled data is required.

6 DISCUSSION AND CONCLUSIONS

Complementary to Bayesian methods, Agatha is developed to disentangle periodic signals from correlated noise. Agatha can select the best noise model and assess the significance of periodic signals based on the BIC-estimated BF. Since it optimizes the correlated noise and trend component for each frequency/period, it presents clearer signals than traditional LS periodograms. Moreover, the MLP-based and BFP-based moving periodograms can be used to diagnose the consistency of signals in time, and to reject false positives.

We test the efficiency of Agatha and the consistency between Agatha and Bayesian methods for an RV challenge data set and the TERRA-reduced HARPS data of HD41248, HD177565 and *CoRoT-7*. Agatha typically identifies signals consistent with those found by Bayesian methods, although it may miss very weak signals due to its assumption of a single signal. Our analysis of RV challenge system 2 is able to recover signals with signal-to-noise ratio down to $K/N = 7.5$, which is probably a limit of reliable detection of planets using the RV method (Dumusque et al. 2017). By quantifying the signals identified by Agatha using the AM algorithm for two interesting nearby stars, we find two new planet candidates with 15.1 and 7.08 M_{\oplus} orbiting HD177565 and HD41248 with periods

of 44.5 and 13.4 d, respectively. The analysis of the HARPS data of HD41248 shows that the previously claimed 26 d signal is probably caused by a combination of planetary perturbation and stellar rotation while the 18.4 d signal is not significant and is an alias of the 13.4 d signal. We also find clues for other short-period signals in the HARPS data of HD177565. We confirm the previous detection of two planets with orbital periods of 0.85 and 3.7 d in the *CoRoT-7* system and provide weak evidence for a signal at a period of 8.9 d.

Compared with previous red-noise periodograms such as Red-Fit (Schulz & Mudelsee 2002) and the compressed sensing periodogram (Hara et al. 2017), the BFP accounts for signals and noise simultaneously and thus avoids the bias introduced by residual analysis. Instead of assuming white noise as Angus et al. (2016) did, Agatha accounts for time-correlated noise and is thus more appropriate for analysing the K2 data to identify stellar rotation periods and to recover acoustic oscillations in giant stars for asteroseismology studies. Moreover, the BFP is the first periodogram that can compare noise models as well as assess signal significance using the BF. To avoid false negatives/positives, the BFP selects the Goldilocks noise model using the BIC-estimated BF. For example, the number of eigen light curves used by Angus et al. (2016) can be optimized by applying the BFP-based model comparison. Otherwise, the eigen light curves, like differential RVs, might introduce additional noise into model fitting (F17). Agatha enables wavelength-dependent noise to be assessed that appears to be an important factor in reliable signal detection.

Nevertheless, the application of Agatha is limited by the assumption of single sinusoidal signal. Thus, it is not aiming at identifying and quantifying signals independently. In addition, we only account for a linear trend in the model while long-period signals are better modelled as a second-order polynomial, although such a linear trend sometimes can improve the fitting significantly. We have used linear functions to model the correlation between RVs and noise proxies, which may not be optimal for the non-linear dependence of RVs on activities as mentioned by Haywood et al. (2016) and Feng et al. (2016). But more sophisticated models may cause the overfitting problem that is mentioned in Feng et al. (2016). Hence, there is no perfect way to model activity-induced RV variation.

To reduce the dimensionality of the model comparison, Agatha compares noise models and signals separately. According to our analyses of HARPS data sets (e.g. F17), the inclusion of periodic functions in the model typically do not change the optimal noise model. Higher order MA model is only necessary if RVs are measured with high cadence (e.g. Tuomi et al. 2013), which usually does not contribute to the RV variation-induced by planets. Hence, the noise and signal selection can be performed separately, although the users can compare the highest BF of BFPs calculated with different noise models to select the optimal combination of signal and noise components.

Considering that Agatha only estimates the significance of a single sinusoidal signal, we suggest to use it in combination with fully Bayesian methods to find periodic signals. Future developments are necessary to generalize Agatha to identify multiple signals with various periodic functions and red-noise models. Agatha is flexible enough to be adapted for time series analyses in various fields such as paleontology (Bailer-Jones & Feng 2013; Feng & Bailer-Jones 2013; Melott & Bambach 2013) and paleoclimatology (Wunsch 2004; Lisiecki 2010; Feng & Bailer-Jones 2015) and particularly in astronomical fields such as quasar variability (Graham et al. 2015; Vaughan et al. 2016), stellar activity (Reinhold, Reiners &

Basri 2013), classification of variable stars (Richards et al. 2011), variability of AGN (Hovatta et al. 2007), solar cycles (Chowdhury, Choudhary & Gosain 2013) and other subjects with periodic signals. We list the following examples specifically.

(i) The LS periodogram has been used to identify various periods in the biodiversity variation (e.g. Melott et al. 2012) while Bayesian methods show no evidence for periodicity (Bailer-Jones 2009; Feng & Bailer-Jones 2013). Instead of subtracting a global trend from the biodiversity time series (Melott et al. 2012), the BFP accounts for a floating trend and thus avoids potential biases introduced by trend-subtraction.

(ii) White-noise periodograms (Graham et al. 2015) and Bayesian methods (Andrae, Kim & Bailer-Jones 2013) have been used to discover periodicity in quasar light curves. To avoid the over-simplified noise model adopted by traditional periodograms and the computationally expensive posterior samplings used by Bayesian methods, the BFP and MLP can be efficiently calculated for a given quasar light curve to disentangle signals from red noise. In addition, the BFP and MLP-based moving periodograms can be used to visualize the change of quasar periodicity in time.

(iii) The LS and GLS have been used to extract periodic features from light curves for the classification of variable stars (Richards et al. 2011; Graham et al. 2013). To improve the classification of variable stars, the BFP/MLP can be calculated for a given light curve in order to account for the red noise, which is found to be common in various light curves (Pont, Zucker & Queloz 2006; Aigrain et al. 2015). Without consideration of a correlated-noise model, the time-correlated noise would probably lead to false positives and neglecting real signals in the light curves, potentially leading to false classifications of variable stars.

(iv) The so-called ‘multiband LS periodogram’ has been developed to extract periodic signals from multiband light curves measured by planned multicolour surveys such as LSST (VanderPlas & Ivezić 2015). However, such a periodogram does not account for wavelength-correlated noise and thus would probably lead to false positives/negatives. Such correlated noise could be modelled by including noise proxies similar to differential RVs in the model.

The Agatha app is made within the SHINY web application framework developed by RSTUDIO (<https://shiny.rstudio.com>). It is aimed at visualizing signals reliably in a framework of periodograms rather than finding periodic signals independently. It should be used in combination with MCMC-based posterior samplings to select and quantify multiple signals. Compared with other periodogram-related softwares, the Agatha app is highly interactive and easy to use, without requiring programming skills. It provides the BFP and MLP together with other periodograms for various applications. On the other hand, the widely used exoplanet software, SYSTEMIC (Meschiari et al. 2009), only provides simple periodograms such as GLS and LS, which could be unreliable for planet detections. PERIOD04 (Lenz & Breger 2004), another periodogram software, only use white-noise periodograms, although it can provide multiple-frequency fits. PLANETPACK (Baluev 2013a), a C++ software, requires knowledge of C++ for usage and is computationally expensive, though it can deal with time-correlated noise and multiple frequencies. Thus, Agatha is a good choice for signal visualization, and would be more versatile if used in combination with Bayesian methods implemented by posterior samplings. Users can use the archived RV data sets or upload their own data to explore signals with Agatha.

ACKNOWLEDGEMENTS

FF, MT and HJ are supported by the Leverhulme Trust (RPG-2014-281) and the Science and Technology Facilities Council (ST/M001008/1). We used the ESO Science Archive Facility to collect RV data sets. We would like to thank the anonymous referee for the valuable comments that significantly improved the manuscript.

REFERENCES

- Aigrain S., Hodgkin S. T., Irwin M. J., Lewis J. R., Roberts S. J., 2015, *MNRAS*, 447, 2880
- Andrae R., Kim D.-W., Bailer-Jones C. A. L., 2013, *A&A*, 554, A137
- Anglada-Escudé G., Butler R. P., 2012, *ApJS*, 200, 15
- Anglada-Escudé G., Tuomi M., 2012, *A&A*, 548, A58
- Anglada-Escudé G., Tuomi M., 2015, *Science*, 347, 1080
- Angus R., Foreman-Mackey D., Johnson J. A., 2016, *ApJ*, 818, 109
- Bailer-Jones C. A. L., 2009, *Int. J. Astrobiol.*, 8, 213
- Bailer-Jones C. A. L., Feng F., 2013, preprint ([arXiv:1307.4266](https://arxiv.org/abs/1307.4266))
- Baluev R. V., 2013a, *MNRAS*, 429, 2052
- Baluev R. V., 2013b, *MNRAS*, 436, 807
- Beichman C. A. et al., 2006, *ApJ*, 652, 1674
- Bretthorst G. L., 2001, in Mohammad-Djafari A., ed., *AIP Conf. Proc. Vol. 568, Bayesian Inference and Maximum Entropy Methods in Science and Engineering*. Am. Inst. Phys., New York, p. 246
- Bruntt H. et al., 2010, *A&A*, 519, A51
- Chowdhury P., Choudhary D. P., Gosain S., 2013, *ApJ*, 768, 188
- Cumming A., 2004, *MNRAS*, 354, 1165
- Cumming A., Marcy G. W., Butler R. P., 1999, *ApJ*, 526, 890
- da Silva R., Porto de Mello G. F., Milone A. C., da Silva L., Ribeiro L. S., Rocha-Pinto H. J., 2012, *A&A*, 542, A84
- Dumusque X., 2016, *A&A*, 593, A5
- Dumusque X. et al., 2017, *A&A*, 598, A133
- Feng F., Bailer-Jones C. A. L., 2013, *ApJ*, 768, 152
- Feng F., Bailer-Jones C. A. L., 2015, *Quat. Sci. Rev.*, 122, 166
- Feng F., Tuomi M., Jones H. R. A., Butler R. P., Vogt S., 2016, *MNRAS*, 461, 2440
- Feng F., Tuomi M., Jones H. R. A. et al., 2017a, *A&A*, preprint ([arXiv:1705.05124](https://arxiv.org/abs/1705.05124), F17)
- Feng F., Tuomi M., Jones H.R.A., Barnes J., Anglada-Escudé G., Vogt S. S., Butler R. P., 2017b, *AJ*, submitted
- Fischer D. A. et al., 2016, *PASP*, 128, 066001
- Ford E. B., Gregory P. C., 2007, in Babu G. J., Feigelson E. D., eds, *ASP Conf. Ser. Vol. 371, Statistical Challenges in Modern Astronomy IV*. Astron. Soc. Pac., San Francisco, p. 189
- Foreman-Mackey D., Montet B. T., Hogg D. W., Morton T. D., Wang D., Schölkopf B., 2015, *ApJ*, 806, 215
- Gilliland R. L., Baliunas S. L., 1987, *ApJ*, 314, 766
- Graham M. J., Drake A. J., Djorgovski S. G., Mahabal A. A., Donalek C., Duan V., Maker A., 2013, *MNRAS*, 434, 3423
- Graham M. J. et al., 2015, *Nature*, 518, 74
- Haario H., Laine M., Mira A., Saksman E., 2006, *Stat. Comput.*, 16, 339
- Hara N. C., Boué G., Laskar J., Correia A. C. M., 2017, *MNRAS*, 464, 1220
- Haywood R. D. et al., 2014, *MNRAS*, 443, 2517
- Haywood R. D. et al., 2016, *MNRAS*, 457, 3637
- Hovatta T., Tornikoski M., Lainela M., Lehto H. J., Valtaoja E., Tornainen I., Aller M. F., Aller H. D., 2007, *A&A*, 469, 899
- Irwin A. W., Campbell B., Morbey C. L., Walker G. A. H., Yang S., 1989, *PASP*, 101, 147
- Jenkins J. S., Tuomi M., 2014, *ApJ*, 794, 110
- Jenkins J. S., Tuomi M., Brasser R., Ivanyuk O., Murgas F., 2013, *ApJ*, 771, 41
- Kass R. E., Raftery A. E., 1995, *J. Am. Stat. Assoc.*, 90, 773
- Léger A. et al., 2009, *A&A*, 506, 287
- Lenz P., Breger M., 2004, in Zverko J., Ziznovsky J., Adelman S. J., Weiss W. W., eds, *Proc. IAU Symp. 224, The A-Star Puzzle*. Cambridge Univ. Press, Cambridge, p. 786
- Levenberg K., 1944, *Q. Appl. Math.*, 2, 164
- Lisiecki L. E., 2010, *Nat. Geosci.*, 3, 349
- Lomb N. R., 1976, *Ap&SS*, 39, 447
- Marquardt D. W., 1963, *SIAM J. Appl. Math.*, 11, 431
- Melott A. L., Bambach R. K., 2013, *ApJ*, 773, 6
- Melott A. L., Bambach R. K., Petersen K. D., McArthur J. M., 2012, *J. Geol.*, 120, 217
- Meschiari S., Wolf A. S., Rivera E., Laughlin G., Vogt S., Butler P., 2009, *PASP*, 121, 1016
- Mortier A., Collier Cameron A., 2017, *A&A*, 601, A110
- Mortier A., Faria J. P., Correia C. M., Santerne A., Santos N. C., 2015, *A&A*, 573, A101
- Pont F., Zucker S., Queloz D., 2006, *MNRAS*, 373, 231
- Queloz D. et al., 2009, *A&A*, 506, 303
- Rajpaul V., Aigrain S., Osborne M. A., Reece S., Roberts S., 2015, *MNRAS*, 452, 2269
- Ramsay G., Hakala P., Wood M. A., Howell S. B., Smale A., Still M., Barclay T., 2016, *MNRAS*, 455, 2772
- Reinhold T., Reiners A., Basri G., 2013, *A&A*, 560, A4
- Richards J. W. et al., 2011, *ApJ*, 733, 10
- Santos N. C. et al., 2014, *A&A*, 566, A35
- Scargle J. D., 1982, *ApJ*, 263, 835
- Schulz M., Mudelsee M., 2002, *Comput. Geosci.*, 28, 421
- Steffen J. H., Hwang J. A., 2015, *MNRAS*, 448, 1956
- Tuomi M., 2012, *A&A*, 543, A52
- Tuomi M., Jenkins J. S., 2012, preprint ([arXiv:1211.1280](https://arxiv.org/abs/1211.1280))
- Tuomi M. et al., 2013, *A&A*, 551, A79
- Tuomi M., Anglada-Escudé G., Jenkins J. S., Jones H. R. A., 2014, preprint ([arXiv:1405.2016](https://arxiv.org/abs/1405.2016))
- VanderPlas J. T., Ivezić, Ž., 2015, *ApJ*, 812, 18
- Vaughan S., Uttley P., Markowitz A. G., Huppenkothen D., Middleton M. J., Alston W. N., Scargle J. D., Farr W. M., 2016, *MNRAS*, 461, 3145
- Wunsch C., 2004, *Quat. Sci. Rev.*, 23, 1001
- Zechmeister M., Kürster M., Endl M., 2009, *A&A*, 505, 859

SUPPORTING INFORMATION

Supplementary data are available at *MNRAS* online.

Table A2. Similar to Table A1 but for HD41248.

Please note: Oxford University Press is not responsible for the content or functionality of any supporting materials supplied by the authors. Any queries (other than missing material) should be directed to the corresponding author for this article.

**APPENDIX: HARPS DATA OF HD177565
AND HD41248**

Table A1. The HARPS data of HD177565. The online version is available at <https://github.com/phillipro/agatha/tree/master/data>. The columns of 3AP2-1 and 3AP3-2 are differential RVs derived from three summations of orders. c3AP2-1 is the calibration data.

JD-2400000	RV (m s ⁻¹)	RV error (m s ⁻¹)	BIS	FWHM	S-index	c3AP2-1 (m s ⁻¹)	3AP2-1 (m s ⁻¹)	3AP3-2 (m s ⁻¹)
52937.514	1.22	0.43	-35.73	6.8160	0.1695	-3.31	-3.31	-1.69
52937.536	0.05	0.43	-34.41	6.8142	0.1683	-0.25	-1.45	-1.27
52939.505	-0.98	0.41	-37.09	6.8150	0.1697	-0.87	-0.32	-2.30
52947.501	0.10	0.40	-37.99	6.8173	0.1715	-2.57	-3.78	-3.51
53146.709	1.68	0.50	-39.28	6.8215	0.1705	-0.13	0.59	-0.05
53146.869	0.86	0.42	-38.31	6.8175	0.1690	-0.59	0.34	0.68
53149.911	4.07	0.50	-34.40	6.8120	0.1685	-0.97	-1.34	-0.48
53150.801	3.34	0.50	-35.30	6.8184	0.1761	-0.19	0.66	-1.08
53154.806	-2.91	0.46	-36.77	6.8131	0.1735	0.05	1.06	3.50
53201.701	-3.40	1.64	-35.00	6.8071	0.1539	0.29	6.53	7.56
53201.705	-0.89	2.06	-29.77	6.8115	0.1526	3.63	3.63	5.97
53201.710	-2.62	2.32	-31.83	6.8018	0.1534	0.24	-2.62	8.56
53202.682	0.93	0.36	-36.53	6.8128	0.1709	-0.48	-0.39	1.13
53202.688	1.21	0.37	-37.39	6.8152	0.1711	-0.53	-1.19	0.25
53203.699	-0.30	0.27	-36.28	6.8213	0.1706	-0.76	-4.20	1.68
53203.704	1.85	0.28	-36.58	6.8192	0.1710	-1.07	-4.05	0.49
53204.660	-4.61	0.35	-36.35	6.8148	0.1706	0.72	3.20	2.44
53204.663	-5.72	0.34	-36.75	6.8146	0.1695	3.57	3.57	3.37
53204.667	-5.13	0.36	-34.60	6.8134	0.1705	0.21	2.54	2.58
53205.577	0.00	0.50	-37.32	6.8159	0.1691	0.27	-1.68	-1.41
53205.579	1.73	0.54	-34.97	6.8140	0.1692	0.40	0.40	0.99
53205.581	0.19	0.50	-34.96	6.8184	0.1700	-0.79	-0.79	-1.14
53205.582	-0.24	0.56	-35.76	6.8140	0.1668	1.48	1.48	-2.10
53205.584	0.50	0.55	-37.78	6.8145	0.1674	0.87	0.40	-0.39
53206.682	-1.80	0.32	-36.29	6.8105	0.1698	0.17	0.70	0.89
53206.686	-0.69	0.32	-35.50	6.8114	0.1699	-0.99	-0.99	2.97
53206.689	-1.24	0.32	-36.17	6.8135	0.1705	-0.29	-0.52	0.43
53217.651	-7.59	0.42	-37.65	6.8090	0.1684	0.15	4.04	1.14
53217.655	-7.40	0.42	-36.01	6.8078	0.1679	0.80	0.80	0.84
53217.659	-7.11	0.44	-35.99	6.8096	0.1685	-0.05	0.82	2.42
53218.686	-0.24	0.40	-36.36	6.8140	0.1692	-0.86	-1.45	-0.44
53218.690	0.71	0.39	-35.94	6.8157	0.1678	-1.20	-1.20	0.15
53218.694	0.11	0.41	-37.54	6.8143	0.1679	0.54	0.26	-0.49
53230.669	2.75	0.38	-36.15	6.8193	0.1703	0.04	-1.39	-1.62
53230.673	2.08	0.36	-36.02	6.8188	0.1694	-1.33	-1.33	0.92
53230.677	0.71	0.38	-35.96	6.8190	0.1711	1.22	-0.66	0.99
53232.626	1.40	0.62	-36.34	6.8173	0.1689	1.18	-0.01	-0.03
53232.630	3.14	0.67	-34.29	6.8149	0.1651	2.19	2.19	-3.03
53232.634	2.21	0.62	-37.20	6.8202	0.1685	-1.25	-0.83	-0.32
53263.578	-3.23	0.28	-37.47	6.8209	0.1681	-1.74	-2.07	1.16
53263.583	-1.14	0.29	-37.65	6.8226	0.1682	-2.04	-2.84	0.89
53264.553	-4.67	0.29	-36.51	6.8191	0.1681	0.51	0.93	3.79
53264.559	-5.37	0.29	-37.03	6.8175	0.1684	-0.85	1.84	4.49
53269.565	-0.48	0.53	-38.85	6.8169	0.1676	-0.02	2.38	-1.10
53269.570	1.01	0.68	-35.30	6.8179	0.1653	0.93	2.80	-0.07
53551.710	2.18	0.30	-33.61	6.8159	0.1808	-0.24	0.29	-1.09
53817.909	4.71	0.33	-30.88	6.8233	0.1859	0.97	-0.12	-2.71
53817.914	4.58	0.31	-30.20	6.8222	0.1856	0.79	0.79	-2.60
54257.771	2.86	0.73	-29.54	6.8394	0.1976	0.76	0.43	4.12
54257.772	4.72	0.69	-29.04	6.8400	0.1930	-0.56	-0.56	-0.17
54257.774	4.28	0.68	-29.43	6.8409	0.1953	3.33	3.33	-1.79
54257.776	4.22	0.65	-30.73	6.8412	0.1925	0.59	0.59	-1.52
54257.777	3.84	0.64	-28.73	6.8405	0.1943	-0.60	-0.27	-0.91
54258.854	4.13	0.68	-28.24	6.8444	0.1922	1.26	1.44	-3.34
54258.856	3.22	0.75	-28.70	6.8475	0.1932	0.97	0.97	-0.77

Table A1 – *continued*

JD-2400000	RV (m s ⁻¹)	RV error (m s ⁻¹)	BIS	FWHM	S-index	c3AP2-1 (m s ⁻¹)	3AP2-1 (m s ⁻¹)	3AP3-2 (m s ⁻¹)
54258.858	3.77	0.73	-30.18	6.8435	0.1945	0.09	0.09	-1.63
54258.860	4.90	0.72	-31.25	6.8448	0.1932	3.05	3.05	-0.55
54258.863	3.00	0.68	-30.68	6.8420	0.1929	-0.18	1.58	0.99
54259.913	4.37	1.31	-31.23	6.8498	0.1867	2.17	-1.55	1.79
54259.916	6.43	1.68	-24.13	6.8417	0.1839	2.17	13.06	-7.10
54259.918	4.30	2.17	-28.72	6.8426	0.1853	-0.29	-0.29	0.80
54259.921	-2.57	2.73	-34.71	6.8590	0.1637	-0.29	11.41	11.11
54259.924	2.63	1.86	-28.04	6.8483	0.1761	4.30	1.68	-0.13
54292.689	0.43	0.33	-28.57	6.8325	0.1933	1.07	1.51	-1.01
54292.695	2.55	0.33	-28.36	6.8329	0.1927	-0.99	0.81	-2.48
54617.853	5.46	0.72	-35.71	6.8369	0.1843	0.88	-0.02	-3.61
54617.858	5.15	0.82	-30.05	6.8382	0.1839	1.31	1.92	-4.95
54621.899	2.27	0.30	-33.66	6.8294	0.1820	-0.06	-0.52	-0.43

Table A2. Similar to Table A1 but for HD41248. The full data set is put online.

JD-2400000	RV (m s ⁻¹)	RV error (m s ⁻¹)	BIS	FWHM	S-index	c3AP2-1 (m s ⁻¹)	3AP2-1 (m s ⁻¹)	3AP3-2 (m s ⁻¹)
52943.85	-1.89	2.13	-35.93	6.72	0.17	-1.29	-1.91	11.42
52989.71	-7.34	3.22	-27.40	6.72	0.16	-2.43	-11.29	15.96
52998.69	-0.22	3.99	-33.53	6.70	0.15	-0.62	15.95	-16.83
53007.68	-2.34	2.21	-28.61	6.72	0.17	3.50	3.50	2.23
53787.61	-4.41	2.63	-31.31	6.72	0.16	0.89	-12.67	0.53
54055.84	-5.49	2.02	-23.95	6.71	0.17	1.26	2.67	4.35
54789.72	-4.79	0.85	-27.43	6.72	0.18	0.27	-1.53	2.25
54790.69	-7.22	0.93	-30.83	6.72	0.17	0.67	0.67	0.42
54791.71	-4.86	0.86	-29.54	6.72	0.18	-2.48	-0.98	1.34
54792.70	-5.02	0.82	-28.09	6.73	0.18	0.08	0.08	0.82
54793.72	-3.35	0.92	-25.28	6.73	0.18	-2.38	0.04	1.53
54794.69	0.04	0.91	-29.59	6.73	0.18	2.71	2.71	-2.06
54795.72	0.48	0.93	-29.54	6.73	0.18	0.75	0.75	-0.54
54796.72	0.51	0.98	-30.33	6.73	0.18	-1.36	-1.36	2.69
54797.71	2.19	0.93	-27.77	6.73	0.18	-1.72	1.31	-1.64
54798.70	3.18	0.93	-25.14	6.73	0.18	-0.06	-4.92	-3.24
...

This paper has been typeset from a \LaTeX file prepared by the author.